

# **Augmin regulates kinetochore tension and spatial arrangement of spindle microtubules by nucleating bridging fibers**

Martina Manenica<sup>1#</sup>, Isabella Koprivec<sup>1#</sup>, Valentina Štimac<sup>1#</sup>, Juraj Simunić<sup>1</sup>,  
Iva M. Tolić<sup>1\*</sup>

<sup>1</sup>Division of Molecular Biology, Ruđer Bošković Institute, Bijenička cesta 54, 10000 Zagreb,  
Croatia

<sup>#</sup>These authors contributed equally to this work.

\*Corresponding author: I.M.T. (tolic@irb.hr)

## ABSTRACT

The mitotic spindle functions as a molecular micromachine that evenly distributes chromosomes into two daughter cells during cell division. A major mechanical element of the spindle are kinetochore fibers attached to sister kinetochores on each chromosome and laterally linked by a bundle of antiparallel microtubules called the bridging fiber. Spindle microtubules are mainly nucleated at the centrosome and on the lateral surface of existing microtubules by the augmin complex. However, it is unknown how the augmin-mediated nucleation affects functionally distinct microtubule bundles and thus the architecture and forces within the spindle. Here we show, by using siRNA depletion and CRISPR knock-out of the augmin complex subunits HAUS6 and HAUS8 in human cells, that augmin is a major contributor to the nucleation of bridging microtubules. Augmin depletion resulted in a ~70% reduction of the microtubule number in bridging fibers and ~40% in kinetochore fibers, suggesting that the bridging microtubules are largely nucleated at the surface of present microtubules. In augmin-depleted cells, the interkinetochore distance decreases preferentially for kinetochores that lack a bridging fiber, independently of the thickness of their k-fibers, indicating that augmin affects forces on kinetochores largely via bridging fibers. Without augmin the number of bridging fibers decreases, with the remaining ones mostly confined to the spindle periphery with an increased overlap length. The reduced number of microtubules also results in a slower poleward flux. Our results demonstrate a critical role of augmin in the formation of bridging microtubules and proper architecture of the metaphase spindle, suggesting a model where sliding of augmin-nucleated bridging microtubules promotes poleward flux of k-fibers and thus tension on kinetochores.

# INTRODUCTION

The mitotic spindle has a highly organized structure that enables it to accurately perform chromosome segregation during cell division. It consists of three major classes of microtubules: kinetochore microtubules that form k-fibers connecting chromosomes to the spindle pole through kinetochores, overlap microtubules that form antiparallel arrays in the central part of the spindle, and astral microtubules that grow from the spindle poles towards the cell cortex (Pavin and Tolić, 2016; Prosser and Pelletier, 2017). During metaphase and early anaphase, overlap microtubule bundles are laterally attached to a pair of sister k-fibers resembling a bridge between them, thus they are called bridging fibers (Kajtez et al., 2016; Vukušić et al., 2017). These fibers balance the tension between sister kinetochores and maintain the curved shape of the metaphase spindle (Kajtez et al., 2016; Polak et al., 2017; Tolic, 2018; Tolic and Pavin, 2016).

Within the spindle of human cells, microtubules are predominantly generated by two nucleation mechanisms: centrosome-dependent and augmin-dependent nucleation (Kirschner and Mitchison, 1986; Prosser and Pelletier, 2017; Wu et al., 2008; Zhu et al., 2008). Centrosome-dependent nucleation was long thought to be predominant in spindle assembly (Prosser and Pelletier, 2017), however, numerous studies revealed that a significant number of microtubules also arises from pre-existing microtubules, through augmin, an eight-subunit protein complex that serves as a recruiter of the  $\gamma$ -TuRC required for microtubule nucleation (David et al., 2019; Goshima et al., 2008; Kamasaki et al., 2013; Lawo et al., 2009; Song et al., 2018; Uehara et al., 2009). Augmin-nucleated microtubules grow at an angle of 0-30° relative to mother microtubules (Kamasaki et al., 2013; Petry et al., 2013; Verma and Maresca, 2019) and show a directional bias towards kinetochores, resulting in the preserved polarity of the spindle once the initial kinetochore-microtubule attachments form (David et al., 2019; Kamasaki et al., 2013). Depletion of augmin complex in different cell types results in impaired k-fiber formation, reduced interkinetochore distance, loss of spindle bipolarity and stability, mitotic delay, and a higher incidence of aneuploidy and cytokinesis failure (Hayward et al., 2014; Uehara and Goshima, 2010; Uehara et al., 2009; Wu et al., 2008; Zhu et al., 2008). Of the eight subunits in the complex, the two directly interacting subunits HAUS6 (hDgt6/FAM29A) and HAUS8 (hDgt4/Hice1) have been the most extensively studied because of their ability to interact with a  $\gamma$ -TuRC adapter protein NEDD1 and pre-existing microtubules, respectively (Song et al., 2018; Uehara et al., 2009). However, how

augmin-dependent microtubule amplification affects functionally distinct microtubule bundles within the spindle and thus its architecture and forces remained unclear.

To explore how the augmin-dependent pathway of microtubule nucleation contributes to the formation of bridging and k-fibers and consequently to forces at kinetochores, we depleted HAUS6 or HAUS8 in hTERT-RPE1 and HeLa cells by using siRNA or CRISPR knock-out technology. We show that the augmin complex plays a vital role in bridging fiber nucleation, ensuring the appropriate forces and the three-dimensional structure of the metaphase spindle. Whereas augmin-mediated nucleation represents the primary nucleation pathway for bridging microtubules, k-fiber microtubules are mainly nucleated through other pathways, most likely at the centrosome. In augmin-depleted cells, the interkinetochore distance decreases preferentially at kinetochores without a bridging fiber, in a manner independent of the thickness of their k-fibers, suggesting an important role of the augmin-generated bridging microtubules in the regulation of interkinetochore tension. Augmin depletion leads to straighter outermost k-fibers and thus a diamond-like shape of the spindle, which is indicative of decreased compression within the k-fibers and demonstrates a role of augmin-generated bridging microtubules in the regulation of spindle forces and shape. Furthermore, without augmin, microtubule poleward flux slows down. We propose that augmin affects tension on kinetochores by generating bridging microtubules from the lateral sides of kinetochore microtubules. The bridging microtubules slide apart, thereby pushing the associated sister kinetochore fibers apart, which promotes poleward flux and tension acting on sister kinetochores.

## RESULTS

### **Bridging microtubules are predominantly generated through augmin-dependent microtubule nucleation**

Bridging fibers are important force-generating and structural elements of the spindle (Kajtez et al., 2016; Vukušić et al., 2017), yet it is not known where and how the microtubules that make up these fibers are nucleated. Centrosomal and augmin-dependent nucleation represent the two main possibilities for the mechanism of bridging fiber formation (Fig. 1A). In the first scenario, future bridging microtubules nucleate at the pole and subsequently make lateral contact to k-fiber microtubules of the same polarity and non-kinetochore microtubules of the opposite polarity extending from the other spindle pole. In the second scenario, previously formed k-fibers serve as an augmin-dependent nucleation site from which bridging microtubules branch off. Recent electron tomography work revealed that minus ends of most bridging fibers reside near k-fibers, supporting the second scenario (O'Toole et al., 2020).

To analyze the contribution of augmin-dependent microtubule nucleation to bridging fiber formation and maintenance, we depleted HAUS6 or HAUS8 components of the augmin complex in hTERT-RPE1 cells stably expressing CENP-A-GFP and centrin1-GFP, stained with SiR-tubulin (Fig. 1B, Supplementary Video 1). Augmin depletion was confirmed using immunocytochemistry (Supplementary Fig. S1A and S1B) and by the previously observed phenotype (Wu et al., 2008; Zhu et al., 2008) of long, curved bundles (Supplementary Video 1). We acquired profiles of tubulin signal intensity along the bundles from metaphase spindles (Fig. 1C) and measured the signal in the central region of the bridging fiber (see Methods). We found that, in comparison with control cells, the bridging fiber was reduced by  $80 \pm 13\%$  and  $51 \pm 18\%$  after HAUS6 and HAUS8 depletion, respectively (Fig. 1D). Moreover,  $26 \pm 6\%$  and  $15 \pm 5\%$  of all kinetochore pairs in HAUS6 and HAUS8 depleted cells, respectively, had no detectable bridging fiber, defined as those with the tubulin signal below the background signal (Fig. 1E; see Methods). These results indicate an important role of the augmin complex in the nucleation of bridging microtubules.

To study the effect of augmin depletion on k-fibers, we measured k-fiber intensity  $1.5 \mu\text{m}$  away from the center of the bridge in the same cells (see Methods) and showed that k-fibers were reduced by  $56 \pm 12\%$  and  $28 \pm 19\%$  after HAUS6 and HAUS8 depletion, respectively (Fig. 1D). Thus, the effect on k-fibers was smaller than on bridging fibers. To check that this result is independent of the method used to analyze tubulin signal intensities, we performed

another type of analysis in which tubulin signal was measured in small regions at the bridge center and next to the kinetochore (see Methods), confirming the result that the bridging fiber was impaired more than k-fibers by augmin depletion (Supplementary Fig. S1C). The analysis of intensity profiles of the bundles in SiR-tubulin stained HeLa cells stably expressing GFP- $\alpha$ -tubulin revealed similarity between the intensity profiles of the two tubulin markers (Supplementary Fig. S1D), suggesting that SiR-tubulin is an appropriate marker for our studies. Taken together, these results suggest that the augmin complex-based nucleation is a major contributor to the formation of bridging fibers, whereas its contribution to the formation of k-fibers is less prominent.

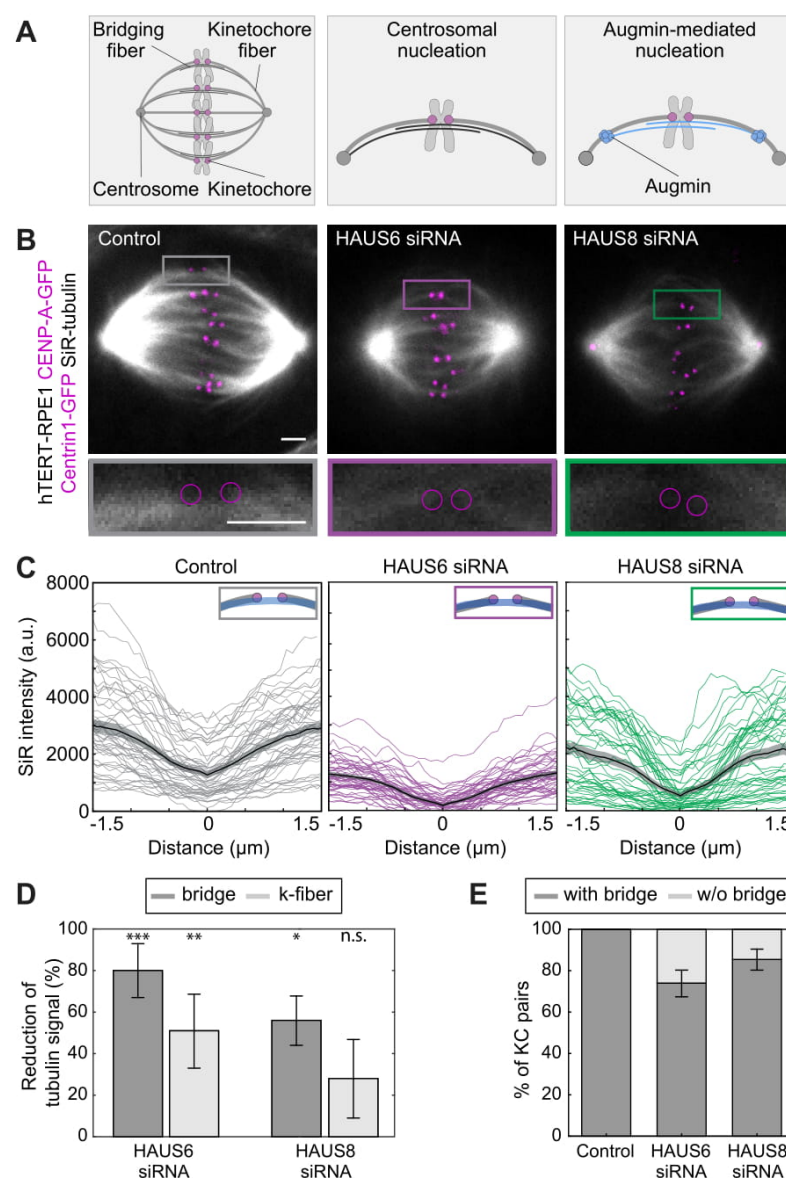


**Figure 1. Severe thinning of bridging fibers caused by augmin complex depletion.** (A) Schematic representation of the mitotic spindle in metaphase (left panel) and two possible pathways of bridging fiber formation - centrosomal nucleation (middle panel, bridging fibers depicted with a black line) and augmin-mediated nucleation (right panel, bridging fibers depicted with a blue line). (B) Live images (single z-plane) of SiR-tubulin (gray) stained metaphase spindles in hTERT-RPE1 cells stably expressing CENP-A-GFP and Centrin1-GFP (both in magenta) in control cells (left) and after HAUS6 (middle) or HAUS8 (right) depletion. Enlarged boxes show bridging fibers affected by HAUS6 or HAUS8 depletion compared to a bridging fiber in control cell. The positions of kinetochores are marked with magenta circles. (C) Intensity profiles of SiR-tubulin signal along the bundles (examples are shown in insets) in control cells (gray) and after HAUS6 (magenta) or HAUS8 (green) depletion. The center of the bridging fiber is set at zero and the minimum intensity of the central part of the spindle was subtracted from the values of intensity profiles. N = 10 cells and 50 bundles for control and HAUS6 siRNA-treated cells, N = 10 cells and 48 bundles for HAUS8 siRNA-treated cells. Mean  $\pm$  SEM (thick black line and shaded area). (D) The observed reduction of tubulin signal in bridging (dark gray) and k-fibers (light gray) following HAUS6 (left) or HAUS8 (right) depletion, values are shown as mean  $\pm$  SEM. p-values were calculated using the absolute values of tubulin signal intensity of bridging or k-fibers following HAUS6 or HAUS8 depletion, compared to the absolute values of tubulin signal intensity of corresponding fibers in control cells. (E) Fractions of kinetochore-pairs with bridging fibers (dark gray) and with no distinguishable bridging fibers (light gray), values are shown as mean  $\pm$  SEM. Statistical analysis (D); t-test, p-value legend: < 0.0001 (\*\*\*\*), 0.0001 to 0.001 (\*\*\*), 0.001 to 0.01 (\*\*), 0.01 to 0.05 (\*),  $\geq$  0.05 (ns). Scale bars, 2  $\mu$ m.

## Shorter interkinetochore distance after augmin depletion is associated with weaker bridging fibers

The interkinetochore distance, which is a readout of interkinetochore tension (Waters et al., 1996), decreases after augmin depletion (Uehara et al., 2009; Zhu et al., 2008). Our measurements on RPE1 and HeLa cells also showed a reduced interkinetochore distance in augmin-depleted cells (Supplementary Fig. S2A-S2D). This reduction of interkinetochore tension may be due to weaker k-fibers (Uehara et al., 2009; Zhu et al., 2008). However, our finding that augmin predominantly nucleates bridging microtubules (Fig. 1) prompted us to hypothesize that the decrease in tension after augmin depletion may result also from weaker bridging fibers.

To test to what extent the observed reduction in interkinetochore distance can be related to the perturbation of bridging fibers in augmin-depleted cells, we divided kinetochore pairs into two groups: (1) those with a bridging fiber (i.e., signal intensity of the bridging fiber > 500 a.u., which corresponds to ~30% of the bridging fiber intensity in control cells), and (2) those with significantly reduced or undetectable signal intensities at the expected locations of



bridging fibers ( $< 500$  a.u.), which we for simplicity refer to as kinetochore pairs without bridging fibers (Fig. 2A, Supplementary Video 2). Remarkably, kinetochore pairs without bridging fibers had a significantly shorter interkinetochore distance than kinetochore pairs with bridging fibers (Fig. 2B). The interkinetochore distance of kinetochores without a bridging fiber was  $0.76 \pm 0.01 \mu\text{m}$  ( $N > 40$  kinetochore pairs from 10 cells) for HAUS6 and  $0.70 \pm 0.02 \mu\text{m}$  ( $N > 40$  kinetochore pairs from 10 cells) for HAUS8 siRNA treated cells. In contrast, kinetochores with a bridging fiber had a distance of  $0.83 \pm 0.02 \mu\text{m}$  ( $N > 40$  kinetochore pairs from 10 cells) and  $0.88 \pm 0.01 \mu\text{m}$  ( $N > 20$  kinetochore pairs from 10 cells) for HAUS6 and HAUS8 depleted cells, respectively (Fig. 2B). While the value of the interkinetochore distance depended on the presence or absence of the bridging fiber, it did not correlate with k-fiber intensity within each group (Fig. 2C). Thus, bridging fibers play a role in regulation of interkinetochore tension in a manner independent of k-fibers.

Next, we explored the spatial distribution of kinetochore pairs with and without bridging fibers. In the inner part of the spindle, less than  $2 \mu\text{m}$  away from the spindle axis, kinetochore pairs with bridging fibers represented only  $32 \pm 6\%$  and  $14 \pm 4\%$  of all kinetochore pairs in HAUS6 and HAUS8 depleted cells, respectively (Fig. 2D). The situation was reversed in the outer part of the spindle, more than  $2 \mu\text{m}$  away from the spindle axis, where kinetochore pairs with bridging fibers represented  $64 \pm 6\%$  and  $65 \pm 7\%$  of all kinetochore pairs following the same treatments (Fig. 2D). To exclude the possibility that this result is affected by the fact that the analysis included only those kinetochores that were well isolated from the neighboring microtubule bundles and thus suitable for tubulin signal measurements, we explored how the interkinetochore distance changes depending on the position of the kinetochore pair within the spindle, for all kinetochores. We found that kinetochore pairs in the outer part of the spindle of cells treated with HAUS6 or HAUS8 siRNA had significantly larger interkinetochore distance than those in the inner part of the spindle (Fig. 2E), which coincides with predominant presence of bridging fibers on the outside (Fig. 2D). These results further support our conclusion that augmin has an important role in regulating interkinetochore tension through nucleation of bridging microtubules.



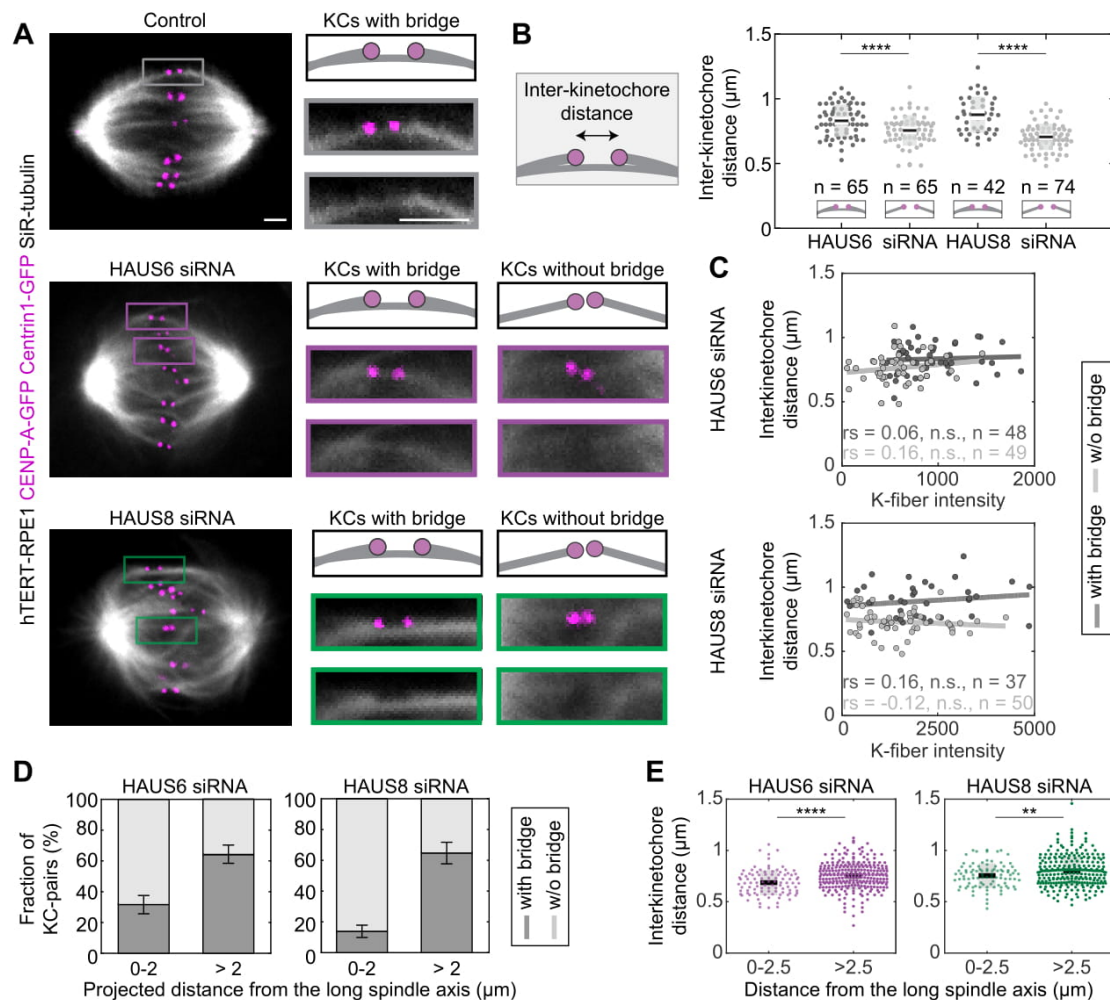


**Figure 2. A reduction in the interkinetochore distance caused by augmin complex depletion is connected with bridging fiber reduction.** (A) Live images (single z-plane) of metaphase spindles in RPE1 cells stably expressing CENP-A-GFP and Centrin1-GFP (both in magenta) and stained with SiR-tubulin (gray). Enlarged boxes show kinetochore (KC) pairs with or without a bridging fiber (see text for definition). Gray frames denote control cells, magenta frames HAUS6 and green frames HAUS8 depleted cells. Brightness and contrast were adjusted for clarity. (B) Univariate scatter plot of the interkinetochore distance in HAUS6 and HAUS8 depleted cells (n=10 cells, n>50 kinetochore-pairs). Kinetochore pairs are divided into two groups: with bridging fiber (dark gray) and without bridging fiber (light gray). (C) Correlation of interkinetochore distance and k-fiber intensity for kinetochore pairs with (dark gray) and without (light gray) bridging fiber in HAUS6 (top) and HAUS8 (bottom) siRNA-treated cells. Data represent a subset from B, in which only kinetochore pairs with k-fibers well-isolated from neighboring microtubules were taken into account. The interkinetochore distance values for kinetochore pairs with and without bridging fibers were  $0.83 \pm 0.02$  and  $0.76 \pm 0.02$   $\mu\text{m}$  for HAUS6 and  $0.89 \pm 0.02$  and  $0.73 \pm 0.01$   $\mu\text{m}$  for HAUS8 siRNA-treated cells, respectively, in agreement with results from panel B. rs, Spearman correlation coefficient. (D) Fractions of kinetochore-pairs with bridging fibers (dark gray) and without bridging fibers (light gray) depending on the projected distance from the long (pole-to-pole) spindle axis in HAUS6 and HAUS8 depleted cells. Fractions are given as mean  $\pm$  SEM. (E) Univariate scatter plot of the

interkinetochore distance in HAUS6 (magenta) or HAUS8 (green) depleted cells depending on the distance from long spindle axis in 3D spindles (light magenta/green for  $<2.5 \mu\text{m}$ , dark magenta/green for  $>2.5 \mu\text{m}$ ). Boxes represent standard deviation (dark gray), 95% confidence interval of the mean (light gray) and mean value (black). Statistical analysis (B and D); t-test, p-value legend:  $< 0.0001$  (\*\*\*\*),  $0.0001$  to  $0.001$  (\*\*\*),  $0.001$  to  $0.01$  (\*\*),  $0.01$  to  $0.05$  (\*),  $\geq 0.05$  (ns). Scale bars,  $2 \mu\text{m}$ .

### **Without augmin overlap bundles are reduced in number, contain a longer overlap region, and are situated at the perimeter of the spindle**

Our finding that the interkinetochore distance and bridging fibers were perturbed more in the inner part of the spindle after augmin depletion prompted us to examine the spatial distribution of bridging fibers and their overlap regions throughout the spindle. We used protein regulator of cytokinesis 1 (PRC1) as a marker because it preferentially crosslinks overlap microtubules (Li et al., 2018; Mollinari et al., 2002), thus providing a specific label for bridging fibers in metaphase spindles (Polak et al., 2017). We analyzed the metaphase spindles by taking a standard "side view" of the spindle and by rotating the 3D image stack of the spindle into an "end-on" view (Fig. 3A) (Novak et al., 2018). HeLa cells stably expressing PRC1-GFP and stained with SiR-DNA after treatment with HAUS6 or HAUS8 siRNA (Fig. 3B, Supplementary Video 3) were used to measure the number of PRC1-GFP bundles, their size and overlap lengths.

We found that the number of PRC1-labeled overlap bundles measured in an end-on view of spindles was almost halved; there were  $20 \pm 2$  distinct bundles in HAUS6 and  $22 \pm 1$  in HAUS8 siRNA treated cells, compared to  $37 \pm 2$  distinct bundles in control cells (Fig. 3C). The analysis of side-view spindle images revealed that the antiparallel overlap regions in HAUS6 and HAUS8 siRNA treated cells were  $8.7 \pm 0.3 \mu\text{m}$  and  $7.2 \pm 0.3 \mu\text{m}$  long, respectively ( $n=50$  overlaps from 10 cells in each case; Fig. 3D). This was twice the length of overlaps in control cells, which were  $4.3 \pm 0.1 \mu\text{m}$  long ( $n=50$  overlaps from 10 cells; Fig. 3D), consistent with previous measurements (Kajtez et al., 2016; Polak et al., 2017). The observed increase in overlap length was not proportional to the increase of spindle length, as overlaps constituted  $39 \pm 1\%$ ,  $69 \pm 4\%$  and  $61 \pm 4\%$  of the spindle length in control cells, HAUS6, and HAUS8 siRNA treated cells, respectively (Supplementary Fig. S3A). Measurements of total PRC1 signal intensity in the spindle revealed that there was no statistically significant difference between control and HAUS6 ( $14 \pm 19\%$  reduction,  $p=0.50$ ) or HAUS8 ( $6 \pm 13\%$  reduction,  $p=0.67$ ) siRNA-treated cells, indicating that there was no

decrease, but only a redistribution of PRC1 within the spindle from a large number of short overlaps to a small number of long overlaps. Interestingly, the long curved bundles characteristic for augmin depletion (Goshima et al., 2008; Uehara et al., 2016; Wu et al., 2008; Zhu et al., 2008) exhibited PRC1 signal along most of their length, suggesting that they consist of antiparallel microtubules, even though contrary to bridging fibers, they form away from the kinetochore fibers and kinetochores (Supplementary Video 1 and 2). These results were corroborated by PRC1-antibody staining in unlabeled HeLa cells, which also showed a reduced number of overlaps and elongated PRC1 signal along the curved outer bundles after augmin depletion (Supplementary Fig. S3B, S3C, S3D), confirming that the observed effects are not a result of PRC1 overexpression. Thus, without augmin, the spindles contain fewer bridging fibers, which have longer overlaps.

The augmin-depleted cells showed a specific spatial distribution of the PRC1-GFP labeled bundles, with more overlap bundles being present around the perimeter of the spindle and fewer in the central part (Fig. 3B "end-on view" and 3E). However, staining with SiR-DNA showed a uniform distribution of DNA throughout the spindle cross-section, both in treated and control cells (Fig. 3B "end-on view"). In agreement with this result, kinetochores and tubulin signal were found uniformly distributed over the spindle cross-section in augmin-depleted and SiR-tubulin stained hTERT-RPE-1 cells stably expressing CENP-A-GFP and centrin1-GFP (Fig. 3B "end-on view" of RPE1 cells). This result indicates that k-fibers are present and roughly uniformly distributed throughout the spindle cross-section and is in agreement with our finding that augmin primarily affects bridging fibers, while k-fibers are less perturbed (Fig. 1).

To explore the role of augmin in defining the overall spindle geometry, we measured spindle length, spindle width as the distance between the outermost microtubule bundles, and the diameter of the metaphase plate as the distance between the outermost kinetochore pairs or the outermost chromosome regions in RPE1 and HeLa cells, respectively (see Methods and scheme in Fig. 4A and C). Spindles of both cell lines were wider in diameter (Fig. 4B and D). Augmin-depleted spindles of HeLa cells were also longer, consistent with previous observations on *Drosophila* S2 cells and *Xenopus* egg extracts (Goshima et al., 2007; Petry et al., 2011). Yet, spindles in RPE1 cells shortened (Fig. 4B and D, Table S1), likely due to differences between cell lines. Interestingly, there was no difference in diameter of the metaphase plate between control and augmin-depleted cells (Fig. 4B and D, Table S1).

Overall, augmin depletion led to the impairment of bridging fibers, which in turn impaired the entire architecture of the metaphase spindle.

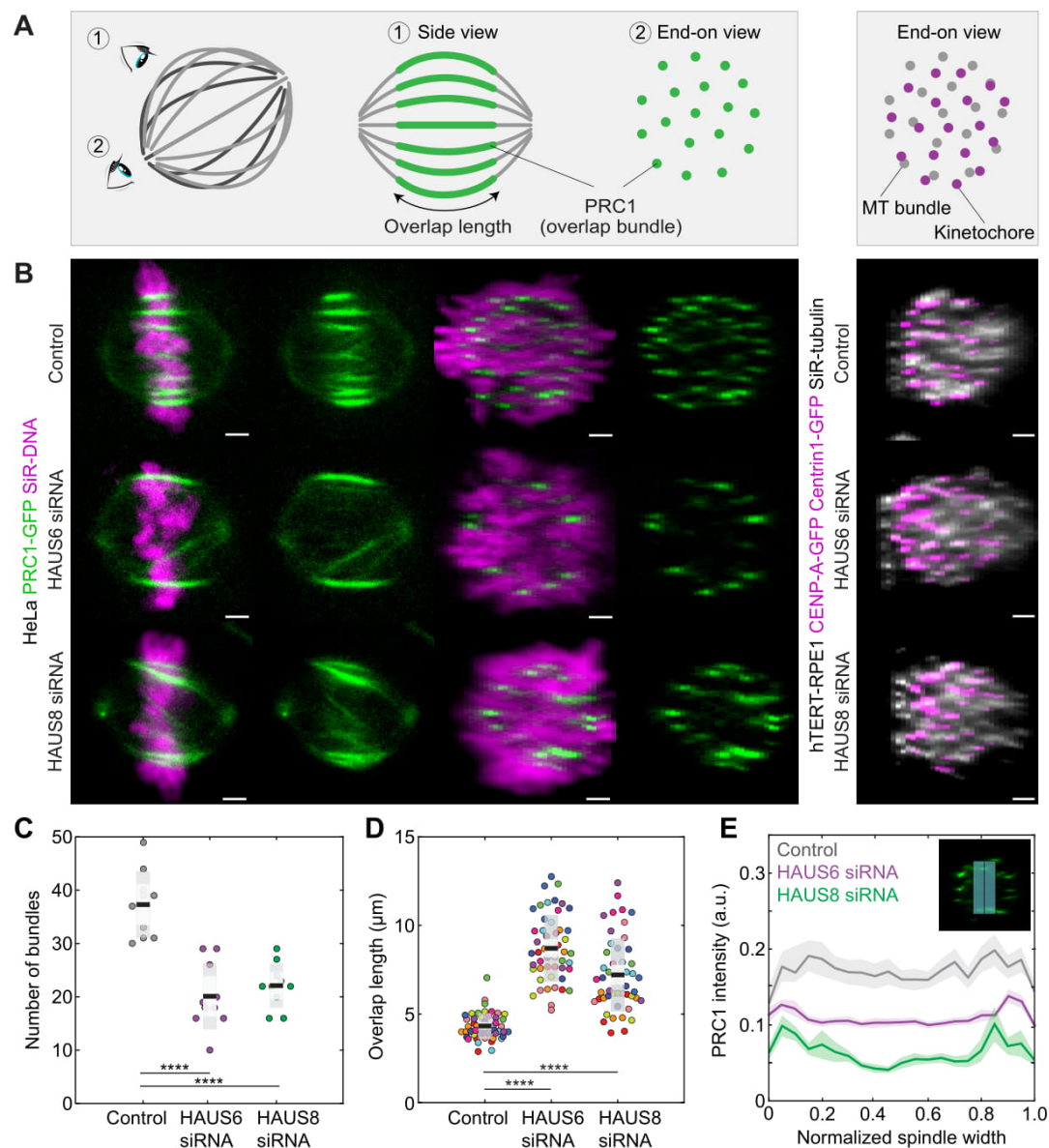


**Figure 3. The specific effects of the augmin complex on overlap bundles.** (A) Schematic representation of a view of the spindle (left panel, gray). Eye signs mark the angle for the side view (1) and the end-on view (2). Side view was used for measuring the length of overlap bundles (green) and end-on view to determine number of bundles (green dots). Schematic representation of an end-on view of RPE1 cells stably expressing CENP-A-GFP and Centrin1-GFP (both in magenta) stained with SiR-tubulin (right panel, gray dots). (B) Columns on the left represent live images of metaphase spindles in HeLa cells stably expressing PRC1-GFP (green) and stained with SiR-DNA (magenta) for chromosomes in control (top) and after HAUS6 (middle) or HAUS8 (bottom) depletion. Left: side view of the spindle; right: end-on view of the same spindle. Right column represents an end-on view of RPE1 cells stably expressing CENP-A-GFP and Centrin1-GFP (both in magenta) and stained with SiR-

tubulin (gray) in control cells (top) and after HAUS6 (middle) and HAUS8 depletion (bottom). Side views are sum projections of 5 central z-slices ( $\Delta z = 0.5 \mu\text{m}$ ) and end-on views are sum projections of 10 central z-slices ( $\Delta z = 0.083 \mu\text{m}$ ). Brightness and contrast were adjusted for clarity. (C) Univariate scatter plot of the number of bundles counted in the end-on view of the spindle. (D) Overlap length measured in the side view of the spindle. Each color in the plot corresponds to data obtained in one cell ( $n=10$  cells and  $n=50$  overlaps). Boxes represent standard deviation (dark gray), 95% confidence interval of the mean (light gray) and mean value (black). (E) Mean PRC1-GFP intensity profile measured in the end-on view of the spindle in control cells (gray) and after HAUS6 (magenta) and HAUS8 (green) depletion. A blue line in the inset marks the measured region (width:  $2.5 \mu\text{m}$ ). Mean (thick lines) and SEM (shaded area). Statistical analysis (C and D); t-test, p-value legend:  $< 0.0001$  (\*\*\*\*),  $0.0001$  to  $0.001$  (\*\*\*),  $0.001$  to  $0.01$  (\*\*),  $0.01$  to  $0.05$  (\*),  $\geq 0.05$  (ns). Scale bars,  $2 \mu\text{m}$ .

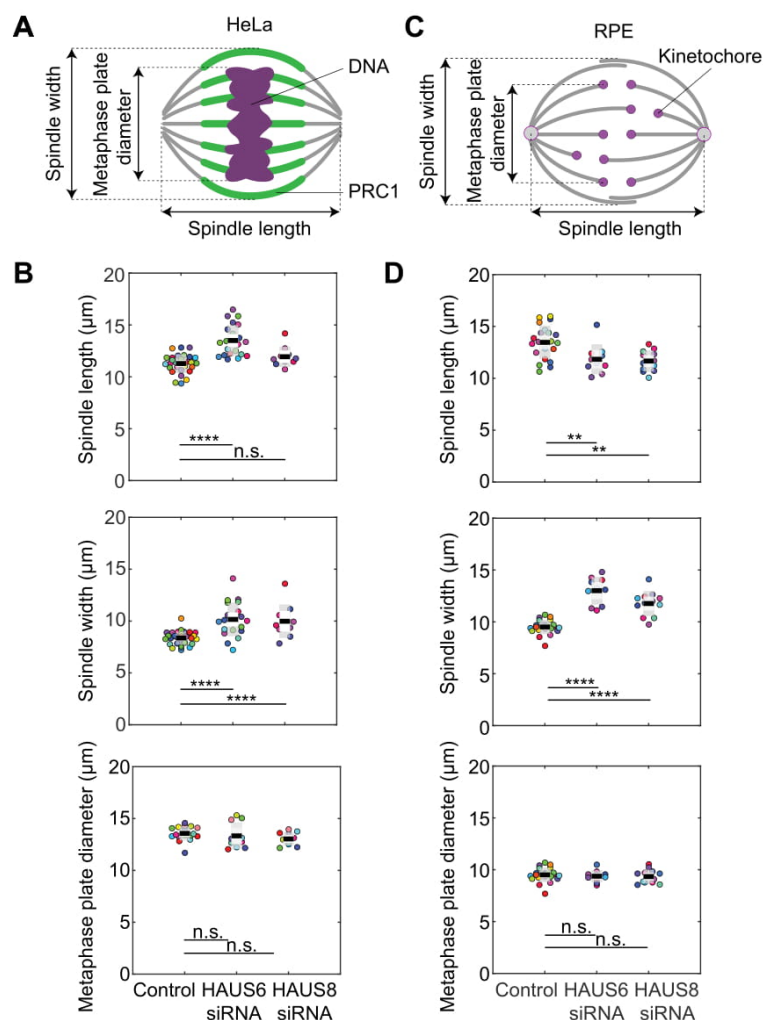


**Figure 4. Spindle length and width were impaired upon augmin depletion, while there was no change in diameter of the metaphase plate.** (A) Schematic representation of HeLa cell stably expressing PRC1-GFP (green) and stained with SiR-DNA (magenta) and (C) RPE1 cell stably expressing CENP-A-GFP and Centrin1-GFP (both in magenta) and stained with SiR-tubulin (gray). Spindle length was measured from pole to pole,



spindle width as a distance between the outermost bundles and diameter of metaphase plate as a distance between outermost chromosome regions (A) or outermost kinetochore pairs (C). (B and D) Univariate scatter plots of the spindle length (top), width (middle) and diameter of metaphase plate (bottom). Each color in the plot corresponds to data obtained in one cell (n= 10 cells). Boxes represent standard deviation (dark gray), 95% confidence interval of the mean (light gray) and mean value (black). Statistical analysis (B and D); t-test, p-value legend: < 0.0001 (\*\*\*\*), 0.0001 to 0.001 (\*\*\*), 0.001 to 0.01 (\*\*), 0.01 to 0.05 (\*),  $\geq 0.05$  (ns).

## **The depletion of augmin leads to straighter k-fibers and excessively long bundles on the spindle periphery**

Augmin-depleted spindles represent a unique system where three types of interactions between k-fibers and bridging fibers can be found within the same spindle: (1) k-fibers attached to bridging fibers, (2) k-fibers without a bridging fiber, and (3) solitary interpolar bundles without associated kinetochores. This is in contrast with control cells, where the first group dominates and the other two groups are rarely found (Polak et al., 2017). To gain insight into the contribution of each of these functionally distinct microtubule bundles to the maintenance of spindle geometry, we explored bundle shapes in HAUS8 siRNA-treated RPE1 cells (Fig. 5A) and in RPE1 cells with induced CRISPR/Cas9 knock-out of HAUS8 (Fig. 5B, Supplementary Video 5). We traced the outermost bundles for each bundle type and compared them with each other as well as with the outermost bundles in control cells (Fig. 5C).

The bundles without kinetochores had the longest contour length, followed by the outermost bundles in control cells, k-fibers with a bridging fiber, and finally, k-fibers without a bridging fiber (Fig. 5D and Table 1). To determine the curvature of the bundles, we fitted a circle to the bundle outline (Supplementary Fig. S4A), and found a drastic reduction of curvature for the k-fibers without bridging fibers in comparison with all other bundle types (Fig. 5E and Table 1). Similar results were obtained in RPE1 and HeLa cell lines treated with HAUS6 siRNA (Supplementary Fig. S4B-S4E and Table 1). Overall, the outer interpolar bundles without associated kinetochores are excessively long and make the spindle wider, whereas k-fibers lacking a bridging fiber are overly straight, ultimately resulting in a diamond-like shape of the spindle. This change in spindle shape is consistent with the prediction of our theoretical model (Kajtez et al., 2016).

**Table 1.** Number and shapes of microtubule bundles in control cells, HAUS6 and HAUS8 siRNA-treated RPE1 cells stably expressing CENP-A-GFP and Centrin1-GFP, hTERT-RPE1 inducible CRISPR/Cas9/HAUS8 knock-out cells and HeLa cells stably expressing PRC1-GFP and CENP-A-mCherry. All tracked bundles are outermost bundles. All values are given as mean  $\pm$  SEM.

Cell line	Treatment	Phenotype	N (bundles)	Contour length ( $\mu$ m)	Radius of curvature/spindle half-length
RPE1	control	outermost bundle	20	$7.5 \pm 0.1$	$1.18 \pm 0.09$
	HAUS6 siRNA	bridge	10	$6.8 \pm 0.1$	$1.7 \pm 0.2$
		no bridge	10	$6.4 \pm 0.2$	$2.0 \pm 0.2$
		no kinetochore	10	$8.2 \pm 0.8$	$1.6 \pm 0.9$
	HAUS8 siRNA	bridge	20	$6.6 \pm 0.5$	$1.30 \pm 0.09$
		no bridge	20	$5.4 \pm 0.3$	$2.4 \pm 0.3$
		no kinetochore	20	$8.2 \pm 0.3$	$1.2 \pm 0.1$
	non-induced KO	outermost bundle	20	$7.1 \pm 0.2$	$1.13 \pm 0.07$
	HAUS8 KO	bridge	20	$5.4 \pm 0.2$	$1.04 \pm 0.08$
		no bridge	20	$5.1 \pm 0.2$	$10 \pm 3$
		no kinetochore	20	$7.7 \pm 0.3$	$0.9 \pm 0.1$
HeLa	control	outermost bundle	20	$6.3 \pm 0.2$	$0.90 \pm 0.05$
	HAUS6 siRNA	bridge	14	$7.7 \pm 0.4$	$1.27 \pm 0.09$
		no bridge	12	$7.1 \pm 0.4$	$7.1 \pm 1.8$
		no kinetochore	10	$10.1 \pm 0.8$	$1.0 \pm 0.2$



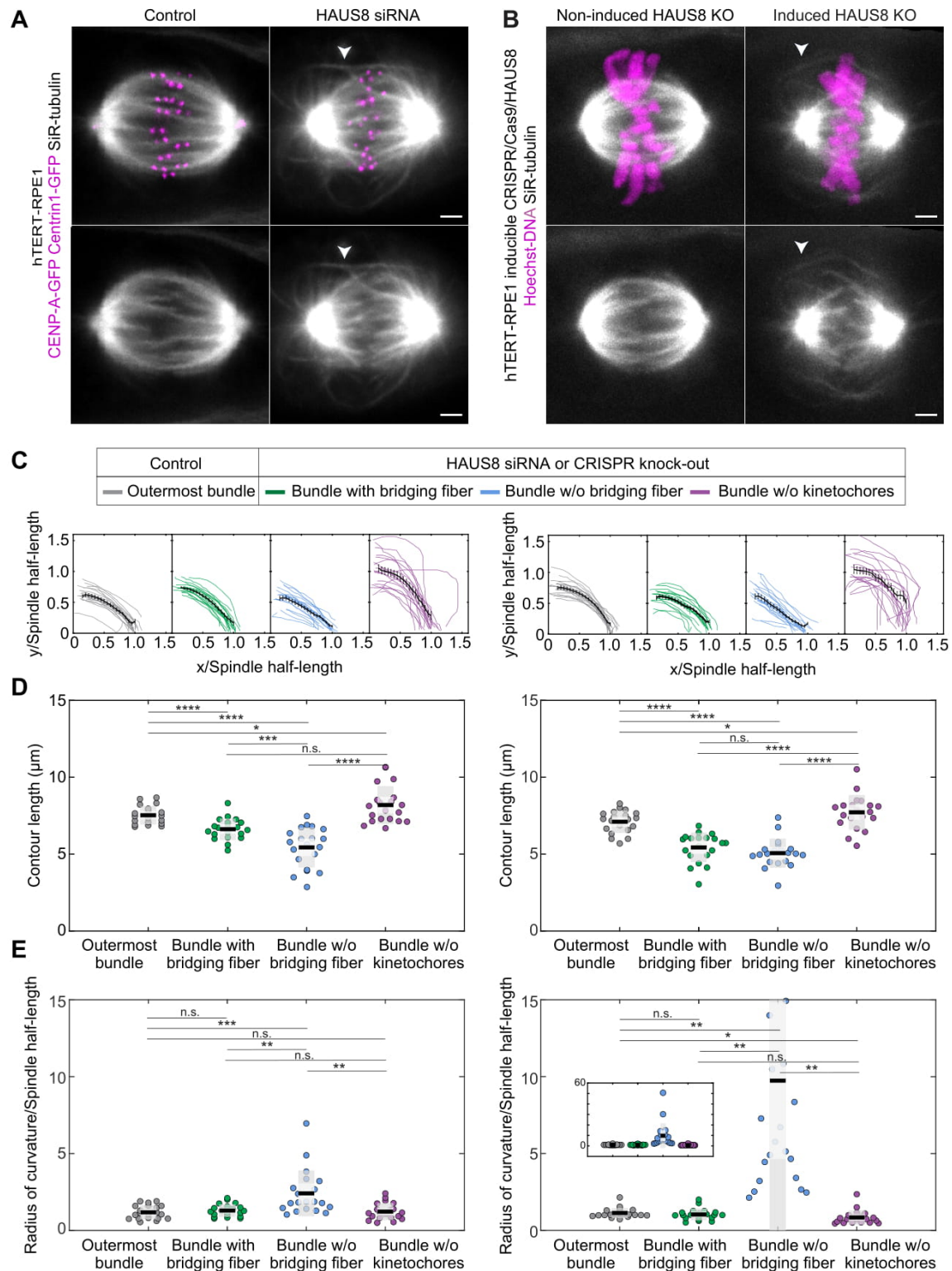


**Figure 5. Bundle shape change upon augmin complex depletion.** (A) Live images (maximum projection of 3 central z-planes) of metaphase spindles in RPE1 cells stably expressing CENP-A-GFP and Centrin1-GFP (both in magenta) and stained with SiR-tubulin (gray). Long curved bundles without kinetochores are marked with a white arrow. (B) Live images (maximum projection of 3 central z-planes) of metaphase spindles in RPE1 inducible CRISPR/Cas9/HAUS8 cells stained with SiR-tubulin (gray) and Hoechst dye (magenta) for

chromosomes. Long curved bundles without kinetochores are marked with a white arrow. (C) Bundle contours in cells from (A) and (B); mean  $\pm$  SEM. (D) Univariate scatter plot of contour lengths and (E) radii of curvature (inset shows an original scale). (C-E) Data on the left corresponds to RPE1 cells stably expressing CENP-A-GFP and Centrin1-GFP and data on the right to RPE1 inducible CRISPR/Cas9/HAUS8 cells. Boxes represent standard deviation (dark gray), 95% confidence interval of the mean (light gray) and mean value (black). Statistical analysis (D and E); t-test, p-value legend:  $< 0.0001$  (\*\*\*\*),  $0.0001$  to  $0.001$  (\*\*\*),  $0.001$  to  $0.01$  (\*\*),  $0.01$  to  $0.05$  (\*),  $\geq 0.05$  (ns). Scale bars,  $2\ \mu\text{m}$ .

## **The absence of augmin slows down microtubule poleward flux**

Sliding of antiparallel microtubules in the central part of the spindle has been proposed to be involved in driving the poleward flux of microtubules (Brust-Mascher et al., 2009; Mitchison, 2005). Yet, the origin of poleward flux is still under debate, as other mechanisms including microtubule depolymerization at the pole and microtubule pushing against chromosome arms are also involved (Ganem et al., 2005; Steblyanko et al., 2020). Because of the significant perturbation of antiparallel bundles in augmin depleted cells, we set out to investigate the influence of augmin depletion on poleward flux (Fig. 6A). In HAUS6 siRNA treated RPE1 cells stably expressing PA-GFP- $\alpha$ -tubulin we observed a decreased photoactivation signal that was more evident in the inner part of the spindle close to the spindle axis (Fig. 6B, bottom time-lapse images and Supplementary Video 5), corresponding to fewer overlap bundles present there (shown in Fig. 3B). Interestingly, the poleward flux rate was reduced from  $2.2 \pm 0.2\ \mu\text{m}/\text{min}$  in control cells to  $1.0 \pm 0.1\ \mu\text{m}/\text{min}$  in HAUS6 siRNA treated cells (Fig. 6C and 6D). This result shows that the impairment of bridging fibers due to augmin depletion affects not only the spindle architecture, but also its dynamics, and suggests a role of augmin-nucleated bridging microtubules in the regulation of poleward flux.

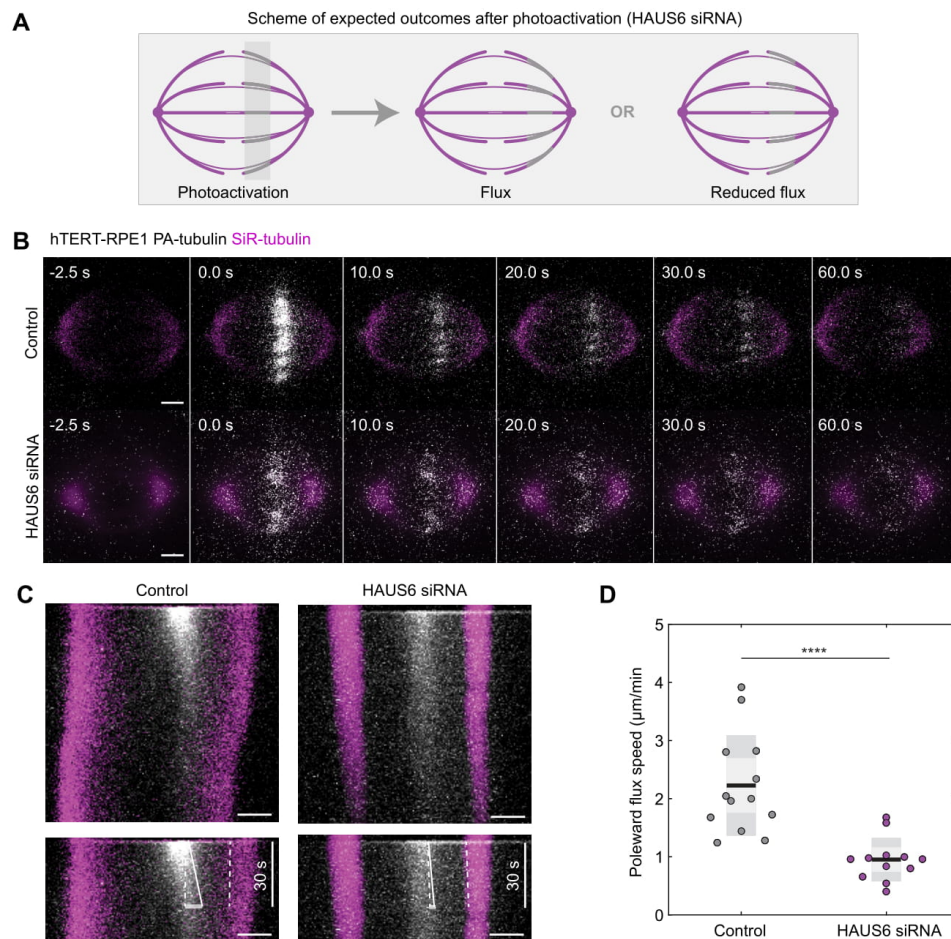


**Figure 6. Augmin complex depletion decreases the poleward flux rate.** (A) Schematic representation of expected outcomes in the spindle (magenta) after photoactivation (gray) in cells depleted of HAUS6. Two outcomes are possible: 1) poleward flux progresses as in control cells (middle) or 2) the flux is reduced (right). (B) Time-lapse images of control (top) and HAUS6 (bottom) depleted RPE1 cells stably expressing PA-GFP- $\alpha$ -tubulin and stained with SiR-tubulin (magenta) before (-2.5 s), at time 0 and after photoactivation (white). (C) Kymograph of the spindles in (B) showing two spindle poles (magenta) and a photoactivation spot (white). Poleward flux speed was measured 30 s after photoactivation (bottom). 1 pt dashed line follows the spindle pole, 1 pt uniform line follows the outer border of the highest tubulin signal trail, 2 pt uniform line was used to obtain the poleward flux speed ( $\Delta x/\Delta t$ ). (D) Univariate scatter plot of the poleward flux speed. Boxes represent standard deviation (dark gray), 95% confidence interval of the mean (light gray) and mean value (black). Statistical analysis; t-test, p-value legend: < 0.0001 (\*\*\*\*). Scale bars, 2  $\mu$ m.

## Discussion

In this paper we provide evidence that the augmin complex is the major contributor to the nucleation and maintenance of bridging fibers. We propose a picture of the metaphase spindle in which bioriented kinetochores are attached to sister k-fibers, and the bridging fiber that spans between them is formed by augmin based nucleation of interpolar bundles that create an antiparallel overlap. Within this overlap, microtubules slide creating a pushing force that the bridging fiber exerts on its k-fibers, thereby contributing to the tension between sister kinetochores. This sliding within the bridging fiber also contributes to the poleward flux by the same mechanism of pushing the k-fibers towards the minus end (Fig. 7).

Involvement of the augmin complex in generation of spindle microtubules has been extensively studied (Song et al., 2018; Uehara et al., 2009), and its depletion has been implicated in several defects of spindle architecture and function, including reduced spindle stability, smaller interkinetochore distance, chromosome misalignment and the formation of long, curved bundles (Hayward et al., 2014; Uehara and Goshima, 2010; Uehara et al., 2016; Uehara et al., 2009; Wu et al., 2008; Zhu et al., 2008). However, the role of augmin-based microtubule nucleation in the origin of bridging fibers has not been studied. Our work shows that the depletion of the augmin complex by silencing the HAUS6 or HAUS8 subunits causes severe thinning of bridging fibers in metaphase spindles, especially in the inner part of the spindle close to the pole-to-pole axis. K-fibers were also thinner, though to a lesser extent. We conclude that the bridging microtubules are predominantly nucleated by the augmin complex along the preexisting microtubules, whereas k-fiber microtubules are nucleated mainly in an augmin-independent manner, most likely by the centrosome. This is in agreement with precious electron microscopy studies of mammalian spindles, where k-fiber microtubules were observed to extend from the centrosome (McDonald et al., 1992), whereas interpolar microtubules, which likely correspond to bridging fibers, start at different points along the k-fiber (Mastrorade et al., 1993.). Moreover, recent electron tomography of human spindles confirmed this result by showing that minus ends of bridging microtubules are found along the k-fiber, less than 50 nm from the k-fiber wall and at a distance 2-4  $\mu$ m from the pole (O'Toole et al., 2020).

Previous work showed that augmin depletion results in a decrease of interkinetochore distance (Uehara et al., 2009; Zhu et al., 2008), a readout of tension, but it was not known if this is due to impaired k-fibers or perturbation of other microtubules. The treatment of cells with a microtubule destabilizing agent, that results in thinner k-fibers, causes a reduction of the

interkinetochore tension (Dudka et al., 2018). However, a similar effect on interkinetochore tension was observed upon perturbation of the bridging fiber by removing the microtubule crosslinker PRC1 (Jagrić et al., 2020; Kajtez et al., 2016; Polak et al., 2017). Our observation that the interkinetochore tension was most severely affected in the inner part of the spindle, where the bridging fibers were most impaired, suggests a connection between interkinetochore tension and augmin-generated bridging fibers. Furthermore, when looking at a subset of kinetochore pairs that had a bridging fiber and those that did not, we found that the tension was more compromised in the latter group. Interestingly, tension was independent of the k-fiber thickness within each group. Although our experiments cannot discern the relative contribution of the bridging and k-fiber impairment in the decrease of tension on kinetochores, they reveal an important and k-fiber independent role of augmin-generated bridging fibers in tension maintenance.

One of the most prominent effects we observed in augmin depleted cells, in addition to the thinning of bridging fibers, was the specific spatial organization of the remaining bridging fibers, which tended to concentrate at the spindle perimeter. At the same time the DNA and kinetochore markers showed that chromosomes are distributed evenly throughout the spindle cross-section in a manner similar to control cells, suggesting that bridging fibers do not strongly influence this distribution of kinetochores. Interestingly, the majority of kinetochore-pairs with reduced bridging fibers are found in the inner part of the spindle close to the long spindle axis, which is in agreement with the spatial distribution of PRC1-labeled bridging fibers preferentially at the spindle periphery. In addition, the overlaps are longer, possibly due to activity of residual PRC1 which crosslinks the remaining microtubules formed by alternative nucleation pathways. Similarly, the extra-long curved interpolar bundles without kinetochores likely arise due to residual PRC1 together with the excess of free tubulin present as a consequence of less tubulin being incorporated in the spindle.

Interestingly, augmin complex depletion results in slower microtubule poleward flux, which supports the model in which poleward flux is largely driven by sliding of antiparallel microtubules (Brust-Mascher et al., 2009; Mitchison, 2005; Miyamoto et al., 2004). The experiments with laser ablation, microneedle pulling, and depletion of crosslinking proteins PRC1 and NuMa showed that the bridging fiber and the k-fibers are tightly linked into a single mechanical element (Elting et al., 2017; Kajtez et al., 2016; Suresh et al., 2020). We hypothesize that the sliding in the bridging fiber transmits force onto the attached sister k-



fibers through this crosslinking and pushes them apart. This contributes to the poleward flux of k-fibers and the interkinetochore tension.

Considering the importance of the interkinetochore tension for the accuracy of cell division (Lampson and Grishchuk, 2017), the maintenance of tension by the bridging fiber might also represent an important mechanism for silencing of the spindle assembly checkpoint (Musacchio and Salmon, 2007; Nicklas et al., 1995; Taylor et al., 1998). As augmin complex depletion causes a higher incidence of aneuploidy (Wu et al., 2008), it would be interesting to see to what extent the impairment of bridging fibers contributes to this issue.

Our results from metaphase open an interesting question about how, during spindle assembly in prometaphase, the bridging fiber and the k-fiber form and come into interaction. The attachment of kinetochores to k-fibers and their biorientation may precede the formation of the bridging fiber, but the kinetochores may also laterally interact with the bridging fiber before the k-fiber forms and kinetochores become bioriented (Simunić and Tolić, 2016). Based on our results, the predominant nucleation of bridging microtubules by augmin indicates a need for preexisting microtubules for their formation, most likely k-fibers. However, since the generation of some bridging microtubules does not depend on augmin, it is also possible that kinetochores laterally interact with these microtubules during early prometaphase. It will be interesting to explore which of these scenarios is used by the cell to build the spindle.

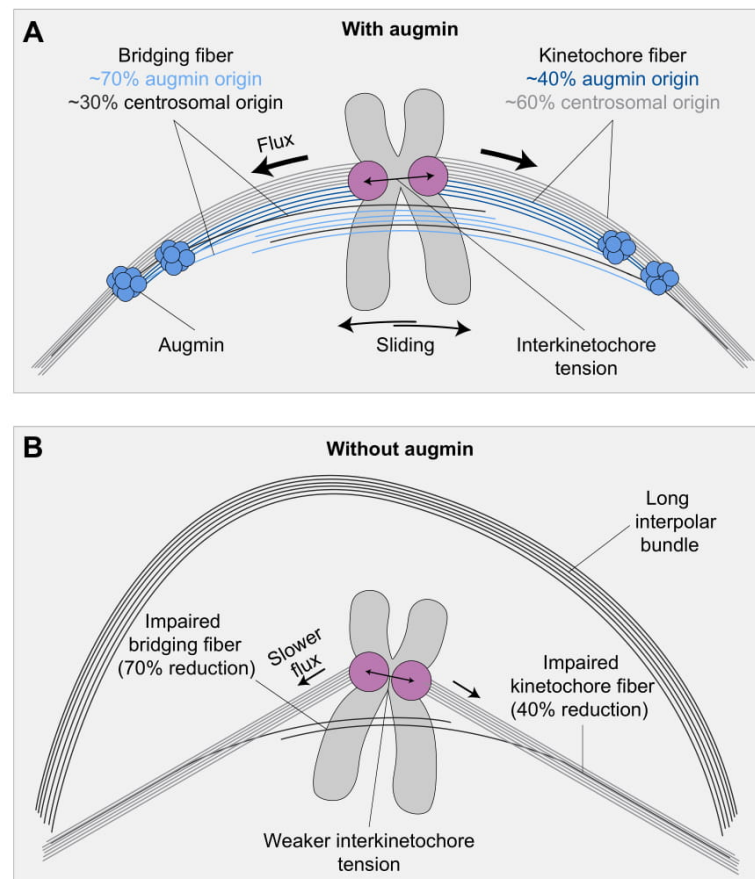


**Figure 7. A model of augmin-dependent nucleation of bridging microtubules and their contribution to interkinetochore tension and poleward flux.** (A) An integrated model of microtubule nucleation: augmin-nucleated microtubules (blue line) and centrosome-nucleated microtubules (gray line) in bridging (light blue and dark gray) and k-fibers (dark blue and light gray). Bridging microtubules are mainly formed by augmin-dependent nucleation. Within their overlaps microtubules slide apart, creating a pushing force onto the k-fibers, thereby contributing to the tension between sister kinetochores and to poleward flux. (B) Microtubules in the absence of augmin complex. Augmin depletion leads to reduction of the microtubule number in the bridging fiber and to a lesser extent in the k-fibers, slower poleward flux, and weaker interkinetochore tension, with the characteristic long interpolar bundles appearing on the spindle periphery.



## MATERIALS AND METHODS

**Cell lines.** Experiments were carried out using unlabeled human HeLa-TDS cells from the High-Throughput Technology Development Studio (MPI-CBG, Dresden); human HeLa-Kyoto BAC cells stably expressing PRC1-GFP, courtesy of Ina Poser and Tony Hyman (MPI-CBG, Dresden, Germany); human HeLa-Kyoto BAC cells stably expressing PRC1-GFP and CENP-A-mCherry, derived from the previously described HeLa-PRC1-GFP cell line using a lentiviral vector system; human HeLa cells stably expressing CENP-A-GFP and centrin1-GFP, which were a gift from Emanuele Roscioli and Andrew McAnish (University of Warwick, Coventry, UK); human HeLa-TDS cells stably expressing GFP- $\alpha$ -tubulin as described in our previous work (Kajtez et al., 2016); human hTERT-RPE-1 (hTERT immortalized retinal pigment epithelium) cells stably expressing CENP-A-GFP and centrin1-GFP, a courtesy of Alexey Khodjakov (Wadsworth Center, New York State Department of Health, Albany, NY, USA); human hTERT-RPE-1 inducible CRISPR/Cas9/HAUS8 knock-out (KO) cells, which were a gift from Iain Cheeseman (Massachusetts Institute of Technology, Cambridge, MA, USA) and human hTERT-RPE-1 cells stably expressing PA-GFP- $\alpha$ -tubulin, a gift from Patrick Meraldi (Faculty of Medicine, University of Geneva, Switzerland).

**Cell culture.** Unlabeled HeLa-TDS cells, HeLa-Kyoto BAC cells stably expressing PRC1-GFP, HeLa-Kyoto BAC cells stably expressing PRC1-GFP and CENP-A-mCherry, human hTERT-RPE-1 cells stably expressing CENP-A-GFP and centrin1-GFP, hTERT-RPE-1 inducible CRISPR/Cas9/HAUS8 KO cells and human hTERT-RPE-1 cells stably expressing PA-GFP- $\alpha$ -tubulin were cultured in flasks in Dulbecco's Modified Eagle's Medium with 1 g/L D-glucose, pyruvate and L-glutamine (DMEM, Lonza, Basel, Switzerland), supplemented with 10% (vol/vol) heat-inactivated Fetal Bovine Serum (FBS, Sigma Aldrich, St. Louis, MO, USA) and penicillin (100 IU/mL)/streptomycin (100 mg/mL) solution (Lonza, Basel, Switzerland). For the selection of HeLa PRC1-GFP, HeLa PRC1-GFP CENP-A-mCherry, HeLa CENP-A-GFP centrin1-GFP and HeLa GFP- $\alpha$ -tubulin cell lines, 50  $\mu$ g/ml geneticin was added to the medium (Life Technologies, Waltham, MA, USA), whereas 500  $\mu$ g/ml G418 was added to the medium for the selection of hTERT-RPE-1 PA-GFP- $\alpha$ -tubulin cell line.

Human hTERT-RPE-1 inducible CRISPR/Cas9/HAUS8 KO cell line was induced every 24 hours for four days using 1  $\mu$ g/ml doxycycline hyclate (Sigma Aldrich, St. Louis, MO, USA), with cells being imaged on the fifth day. All cells were kept at 37°C and 5% CO<sub>2</sub> in a Galaxy 170 R humidified incubator (Eppendorf, Hamburg, Germany). All cell lines have been

regularly tested for mycoplasma contamination by examining the samples for extracellular DNA staining with SiR-DNA (100 nM, Spirochrome, Stein am Rhein, Switzerland) and Hoechst 33342 dye (1 drop/2 ml of NucBlue Live ReadyProbes Reagent, Thermo Fisher Scientific, Waltham, MA, USA) and have been confirmed to be mycoplasma free.

**Lentiviral cell transfection.** For stable expression of CENP-A in HeLa PRC1-GFP cells, a lentiviral transduction was used. Lentivirus was produced in HEK-293 cells by cotransfection of the cells with pLenti6-CENP-A-mCherry (No. 89767, Addgene) plasmid carrying blasticidin selection, pSPAX2 (No. 12260, Addgene) and pCMV-VSV-G (No. 8454, Addgene) plasmids. After 36 and 72 hours, the culture medium containing lentivirus particles was harvested and added to HeLa cells stably expressing PRC1-GFP. After the second treatment, HeLa cells were cultured for six weeks under blasticidin selection prior to being used for imaging.

**Sample preparation and RNAi transfection.** At 80% confluence, DMEM medium was removed from the flask and cells were washed with 5 ml of PBS. Then, 1 ml 1% trypsin/EDTA (Biochrom AG, Berlin, Germany) was added to the flask and cells were incubated at 37°C and 5% CO<sub>2</sub> in a humidified incubator for five minutes. After the incubation, trypsin was blocked by adding 2 ml of DMEM medium. For RNAi experiments, the cells were seeded to reach 60% confluence the next day and cultured on 35 mm uncoated dishes with 0.16-0.19 mm (1.5 coverglass) glass thickness (MatTek Corporation, Ashland, MA, USA) in 2 mL DMEM medium with previously described supplements. After one day of growth, cells were transfected with either targeting or non-targeting siRNA constructs which were diluted in OPTI-MEM medium (Life Technologies, Waltham, MA, US) to a final concentration of 20 nM. All transfections were performed 48 hours prior to imaging using Lipofectamine RNAiMAX Reagent (Life Technologies, Waltham, MA, US) according to the instructions provided by the manufacturer. After four hours of treatment, the medium was changed to the previously described DMEM medium. The constructs used were human HAUS6 siRNA (L-018372-01-0005, Dharmacon, Lafayette, CO, USA), human HAUS8 siRNA (L-031247-01-0005, Dharmacon, Lafayette, CO, USA) and control siRNA (D-001810-10-05, Dharmacon, Lafayette, CO, USA).

In order to visualize microtubules, all cells except HeLa PRC1-GFP and HeLa GFP- $\alpha$ -tubulin cells were stained to a final concentration of 100 nM with a far-red silicon rhodamine (SiR)-tubulin-670 dye (Spirochrome, Stein am Rhein, Switzerland), 45 minutes to 2 hours prior to imaging. In order to avoid dye efflux, a broad-spectrum efflux pump inhibitor verapamil

(Spirochrome, Stein am Rhein, Switzerland) was added at a final concentration of 0.5  $\mu$ M to hTERT-RPE-1 cells along with SiR-tubulin. For chromosome visualization, HeLa PRC1-GFP and HeLa GFP- $\alpha$ -tubulin cells were stained with 100 nM SiR-DNA dye for 20 minutes to 2 hours prior to imaging. hTERT-RPE-1 PA-GFP- $\alpha$ -tubulin cells were stained with 25 nM SiR-tubulin for 3 hours prior to imaging and hTERT-RPE-1 inducible CRISPR/Cas9/HAUS8 KO cells were stained with 1 drop of Hoechst 33342 dye (Thermo Fisher Scientific, Waltham, MA, USA) in 2 mL of DMEM medium.

**Immunocytochemistry.** HeLa cells stably expressing PRC1-GFP were grown on glass-bottomed dishes (14 mm, No. 1.5, MatTek Corporation) and fixed by 2 ml of ice-cold methanol for 1 min at -20°C. Following fixation, cells were washed 3 times for 5 minutes with 1 ml of PBS. To block unspecific binding, cells were incubated in 1 ml blocking/permeability buffer (1% normal goat serum (NGS) and 0.5% Triton-X-100 in water) for 30 minutes at 4°C. Cells were then washed 3 times for 5 minutes with 1 ml of PBS and incubated with 250  $\mu$ l of primary antibody solution overnight at 4°C. The primary antibodies used were as follows: rabbit polyclonal PRC1 (diluted 1:100, sc-8356, Santa Cruz Biotechnology) and rabbit polyclonal HAUS6 (diluted 1:250, ab-150806, Abcam). After the incubation with a primary antibody, cells were washed 3 times for 5 minutes with 1 ml of PBS and then incubated with 250  $\mu$ l of secondary antibody for 45 minutes at a room temperature. Alexa Fluor 488 and 594 (Abcam) were used as secondary antibodies at a 1:1000 dilution for PRC1 staining and 1:500 dilution for HAUS6 staining.

**Microscopy.** Cells were imaged using a previously described microscope setup (Buda et al., 2017), consisting of a Bruker Opterra Multipoint Scanning Confocal Microscope (Bruker Nano Surfaces, Middleton, WI, USA), mounted on a Nikon Ti-E inverted microscope with a Nikon CFI Plan Apo VC 100x/1.4 numerical aperture oil objective (Nikon, Tokyo, Japan). During live-cell imaging, cells were kept at 37°C and 5% CO<sub>2</sub> in Okolab Cage Incubator (Okolab, Pozzuoli, NA, Italy). To excite Hoechst, GFP, mCherry or SiR fluorescence, a 405 nm, 488 nm, 561 nm or 647 nm laser lines were used, respectively. Opterra Dichroic and Barrier Filter Set 405/488/561/640 enabled the separation of excitation light from the emitted fluorescence. Images were acquired using Evolve 512 Delta Electron Multiplying Charge Coupled Device (EMCCD) Camera (Photometrics, Tuscon, AZ, USA), with camera readout mode of 20 MHz. The xy-pixel size was 83 nm. In all experiments where the whole spindle stack was imaged, z-stacks were acquired with unidirectional xyz scan mode at 37 focal planes and 0.5  $\mu$ m distance between planes. For time lapse imaging, a single z plane was

acquired every 0.5 seconds. Photoactivation was performed perpendicular to pole-to-pole axis of metaphase spindles using a 405-nm laser diode (Coherent, Santa Clara, CA, USA) and a line pattern of 12 equally distributed points, with each point representing one laser hit. The interval between the points was 0.05 ms and photoactivation area was set to 0.5  $\mu\text{m}$  for each point. The interval between successive frames was set to 0.5 s, one central z-plane was imaged and 160 successive frames were recorded, thereby obtaining an 80 s time lapse for each cell.

**Image processing and data analysis.** In cells where HAUS6 or HAUS8 were silenced only bipolar metaphase spindles were imaged and analyzed, even though multipolar spindles were observed as reported previously (Lawo et al., 2009). For experiments that included a transformation of spindles into the end-on view, only cells that had spindles with both poles approximately in the same plane were imaged and analyzed. All images were analyzed in Fiji/ImageJ (National Institutes of Health, Bethesda, MD, USA). Raw images were used for quantification and contrast was adjusted for clarity for representation on figures. MatLab (MathWorks, Natick, MA, USA) was used to create the plots, Rstudio (R Foundation for Statistical Computing, Vienna, Austria) to transform the cells into an end-on view and Python to fit the circles to determine the curvature of bundles. Figures were assembled in Adobe Illustrator CS5 (Adobe Systems, Mountain View, CA, USA).

**Measuring the bridging fiber intensity.** Tubulin intensity of a bridging fiber and k-fiber region was measured in a single z plane using the Segmented Line tool by drawing the 5 pixel line along the contour of k-fibers and the corresponding bridging fiber. Background was measured in the same z plane by drawing the 5 pixel line along the length of the metaphase midzone, as this represents the background signal caused by the presence of neighboring microtubules. The minimum value of the midzone intensity profile was subtracted from the intensity profiles of bundle contours. The minimum value of the mean intensity profile was set as a distance of 0  $\mu\text{m}$  and was selected as the center of the bridging fiber. A MatLab script was used to acquire the mean intensity profile of all single bundle intensity profiles. The final intensity of a bridging fiber was calculated as the mean value of intensities in the area 500 nm around the center of the bridging fiber. The final intensity of a k-fiber region was calculated as an average of two mean values of intensities in the area 500 nm around the distance of 1.5  $\mu\text{m}$  away from the center of the bridging fiber. Additionally, tubulin intensity in bridging and k-fibers was measured using a 5x5 pixel Square tool. To measure bridging fibers, the square was positioned on the fiber spanning the area between two kinetochores. K-fibers were

measured right next to the kinetochores. The average intensity of the two sister k-fibers was used for further analyses. The background was measured using the same tool right above and below the bridging fiber and the average intensity of the two spots was subtracted from bridging and k-fiber intensities.

**Comparison of SiR- and GFP-tubulin signal.** For the comparison of SiR and GFP-tubulin signal in HeLa cells stably expressing GFP- $\alpha$ -tubulin, the previously described analysis was used. Tubulin intensity of a bridging fiber and k-fiber region was measured in a single z plane using the Segmented Line tool by drawing the 5 pixel line along the contour of k-fibers and the corresponding bridging fiber. Due to high noise, only outermost bundles were taken into analysis and the reduction was not calculated. The background was measured in the same z plane by drawing the 5x5 pixel square in the cytoplasm and was subtracted from the bundle intensity profiles. The minimum value of the intensity profile was set as a distance of 0  $\mu$ m and was selected as the center of the bridging fiber.

**The interkinetochore distance.** The interkinetochore distance was measured in ImageJ using a Point tool, after the images were rotated to make the spindle parallel to x-axis. Two points were put on spindle poles and two points on the upper and lower edge of the metaphase plate. Additional two points were put on the centers of signal in each kinetochore pair. Interkinetochore distance and distance from spindle axes were calculated using a home-written MatLab script. Two-dimensional analysis was applied when all tracked kinetochore pairs resided within 2  $\mu$ m around the central z-plane, which was determined as the plane in which both centrosomes were clearly visible. Three-dimensional analysis was used when all kinetochore pairs in the spindle were taken into account, regardless of their position. In 2D analysis, Line tool was used to measure the projected distance of a middle point between two sister kinetochores in a particular z-plane from the long spindle axis. In 3D analysis, the exact distance from the long spindle axis (c) was calculated using the Pythagorean theorem, where a= projected distance of a middle point between two sister kinetochores in a particular z-plane from the long spindle axis, b = distance between the central z-plane and the z-plane of the kinetochore pair x 0.81 (correction factor, see Transformation of spindles into a end-on view). Additionally, kinetochores with visible bridging fibers and kinetochores with no visible bridging fibers were separately tracked and analyzed in hTERT-RPE-1 cells stably expressing CENP-A-GFP and centrin1-GFP. The presence of bridging fibers was determined by measuring intensity profiles of the tubulin signal between two kinetochores.

**Transformation of spindles into an end-on view.** Z-stacks of the mitotic spindles that were positioned horizontally were transformed into the end-on view using a home-written R script previously described in our work (Novak et al., 2018). Prior to transformation, a single-channel grayscale z-stack was rotated using ImageJ to make the long axis of the spindle parallel to the x-axis. Signal intensity at each pixel was used to acquire an end-on view of the spindles by applying the following transformation:  $I'(i \cdot \Delta \text{pixel size}, j \cdot \Delta \text{pixel size}, k \cdot \Delta \text{z-distance}) = I(k \cdot \Delta \text{z-distance}, i \cdot \Delta \text{pixel size}, j \cdot \Delta \text{pixel size})$ . In the transformation,  $ijk$  coordinates correspond to 3D positions and a correction factor of 0.81 was used to ensure that the z-distance was correct, taking into account aberrations caused by a different refractive index of aqueous samples and immersion oil (Novak et al., 2018).

**Number of bundles.** The number of bundles in HeLa-PRC1-GFP cells was determined in an end-on view of the spindle by using sum intensity projections of ten central z-planes covering 0.83  $\mu\text{m}$  along the long spindle axis. Intensity profiles of PRC1-GFP were measured on the same sum intensity projections by drawing a 50-pixel wide Straight line tool across the diameter of the spindle.

**Spindle length, width and metaphase plate diameter.** Spindle length, width and metaphase plate diameter were measured on maximum intensity projections of the side view z-stack. Spindle length was determined in ImageJ by drawing the line from pole to pole using the Straight line tool. The position of the poles was determined as either the center of centrin1 signal or the outermost points of the tubulin signal at the spindle pole. Spindle width was measured as the distance between two lines parallel to the long axis of the spindle and encompassing the outermost PRC1- or tubulin-labeled bundles. Additionally, in hTERT-RPE-1 cells stably expressing CENP-A-GFP and centrin1-GFP the metaphase plate diameter was measured as the distance between the outermost kinetochore pairs, whereas in HeLa PRC1-GFP it was measured as the distance between the outermost chromosome ends after specifying the metaphase plate using Square Tool.

**Overlap length.** Overlap length was measured on sum intensity projections of 2 to 4 z-planes covering the bundle of interest, using ImageJ Segmented line tool by drawing a pole-to-pole line along the contour of PRC1-GFP and acquiring an intensity profile. The overlap length was defined as the length of the base of the PRC1-GFP intensity peak (Polak et al., 2017).

**PRC1 intensity.** PRC1 intensity was measured in sum intensity projections of all z-planes covering the whole spindle. Total PRC1 signal in the cell was marked by using Polygon



selection tool and 5x5 Square tool was used to determine the background in the cytoplasm. The final intensity values were obtained using the following formula:  $\text{PRC1 intensity} = \text{Integrated Density of the spindle} - (\text{Area of selected cell} \times \text{mean fluorescence of background})$ .

**Spindle shape.** The shape of spindles was determined in ImageJ using a Point tool. The images were rotated to make spindles parallel to the x-axis. A line that goes from the top to the bottom of a metaphase plate and a pole-to-pole line were drawn using Line tool. The meeting point of the lines was defined as a middle point of the spindle. Then, one point was put in the middle of the spindle, two points on spindle poles and two points on the upper and lower edge of the metaphase plate. Additional points were used to track the outermost bundle contours at least 2.5  $\mu\text{m}$  away from the long spindle axis in single z-slices. The first point of the bundle was at a spindle pole and the last point was either next to the kinetochore or at half of the long spindle axis. The outermost bundle was tracked in control cells. In treated cells, three different groups of outermost bundles were tracked: bundles with visible bridging fibers, bundles with no visible bridging fibers and curved bundles extending far from the metaphase plate. Shape and curvature were calculated using a home-written Python script based on a previously published method (Kanatani and Rangarajan, 2011). Contour lengths of the bundles were measured by calculating the distance between the first and the last point of the tracked bundle.

**Poleward flux rate.** To measure the poleward flux, a line covering the whole spindle was drawn from pole to pole using the Line tool. Kymograph Builder was used to obtain kymographs and poleward flux was measured as previously described (Preira and Maiato, 2010) during the first 30 seconds after photoactivation along the outer border of the highest intensity signal trail and towards the closest spindle pole.



## Acknowledgements

We thank Alexey Khodjakov for the RPE1 CENP-A-GFP Centrin1-GFP cell line, Ina Poser and Tony Hyman for the HeLa PRC1-GFP cell line, Emanuele Roscioli and Andrew McAinsh for the HeLa CENP-A-GFP Centrin1-GFP cell line, Mariola Chacon for the HeLa-TDS cell line, Iain Cheeseman for the RPE1 inducible CRISPR/Cas9/HAUS8 KO cell line and Patrick Meraldi for the RPE1 PA-GFP- $\alpha$ -tubulin cell line, Arian Ivec for help with the shape analysis, Josip Čačković for technical assistance, all members of Tolić and Pavin groups for discussions and advice, Ivana Šarić for help with the drawings. This work was funded by the European Research Council (ERC Consolidator Grant, GA number 647077), Croatian Science Foundation (Project IP-2014-09-4753), Croatian Science Foundation Cooperation Programme with Croatian Scientists in Diaspora “Research Cooperability” (Project PZS-2019-02-7653) and QuantiXLie Centre of Excellence, a project cofinanced by the Croatian Government and European Union through the European Regional Development Fund - the Competitiveness and Cohesion Operational Programme (Grant KK.01.1.1.01.0004).

## Author Contribution

M.M., I.K. and V.Š. performed the experiments, analyzed the data and assembled the figures. J.S. performed lentivirus-based cell line construction. V.Š. and I.K. wrote the manuscript with input from M.M, J.S. and I.M.T. The experiments were conceived by J.S. and I.M.T. I.M.T. supervised the project.

## Competing Interests

The authors declare no competing interest.

## Data Availability

All data are available from the corresponding author upon request.

## Code Availability

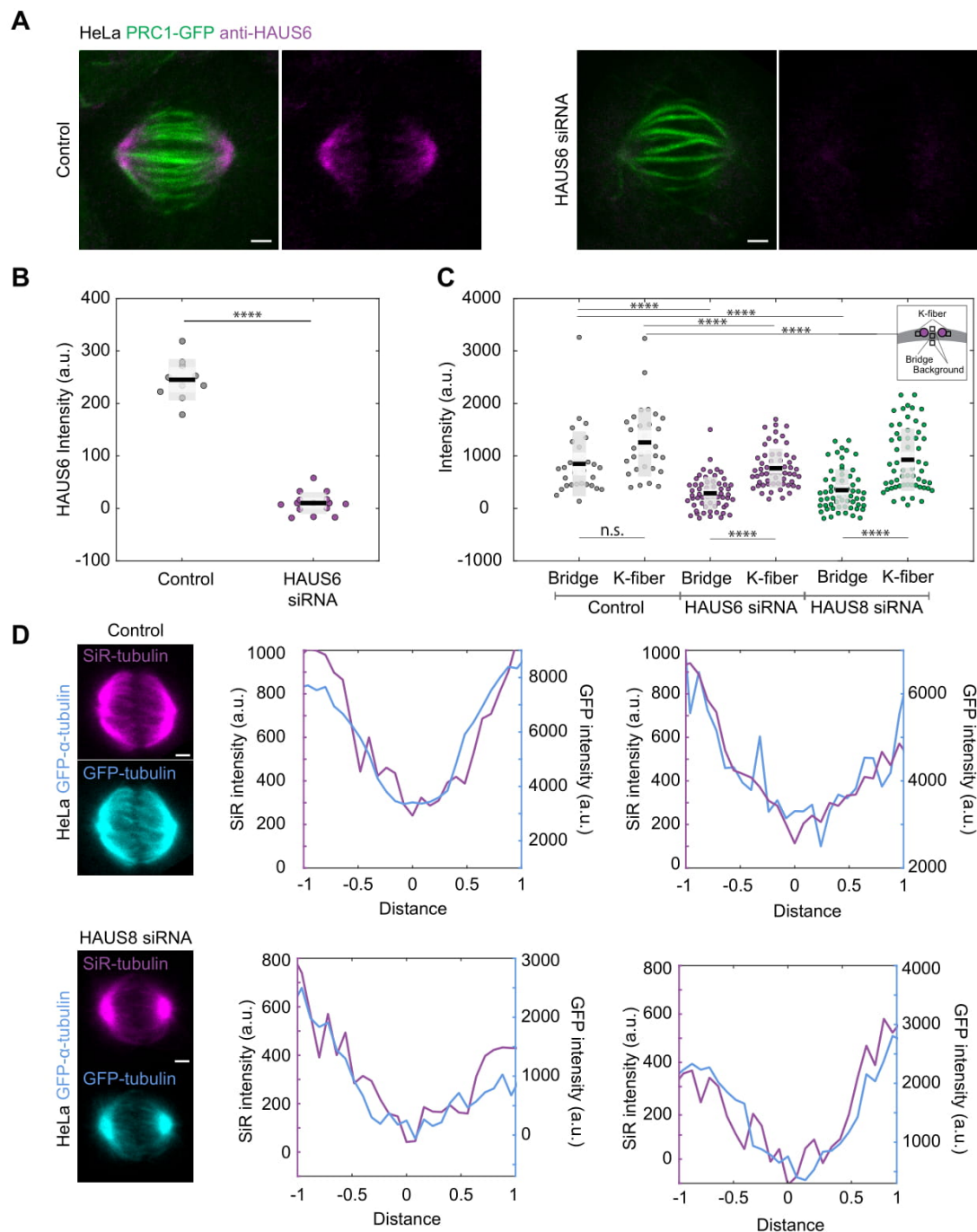
All scripts used in this study are available upon request.

## Supplementary Tables

**Table S1.** Spindle lengths, widths and diameters of the metaphase plate in control cells, HAUS6 and HAUS8 siRNA-treated HeLa cells stably expressing PRC1-GFP and hTERT RPE1 cells stably expressing CENP-A-GFP and Centrin1-GFP. All values are given as mean  $\pm$  SEM.

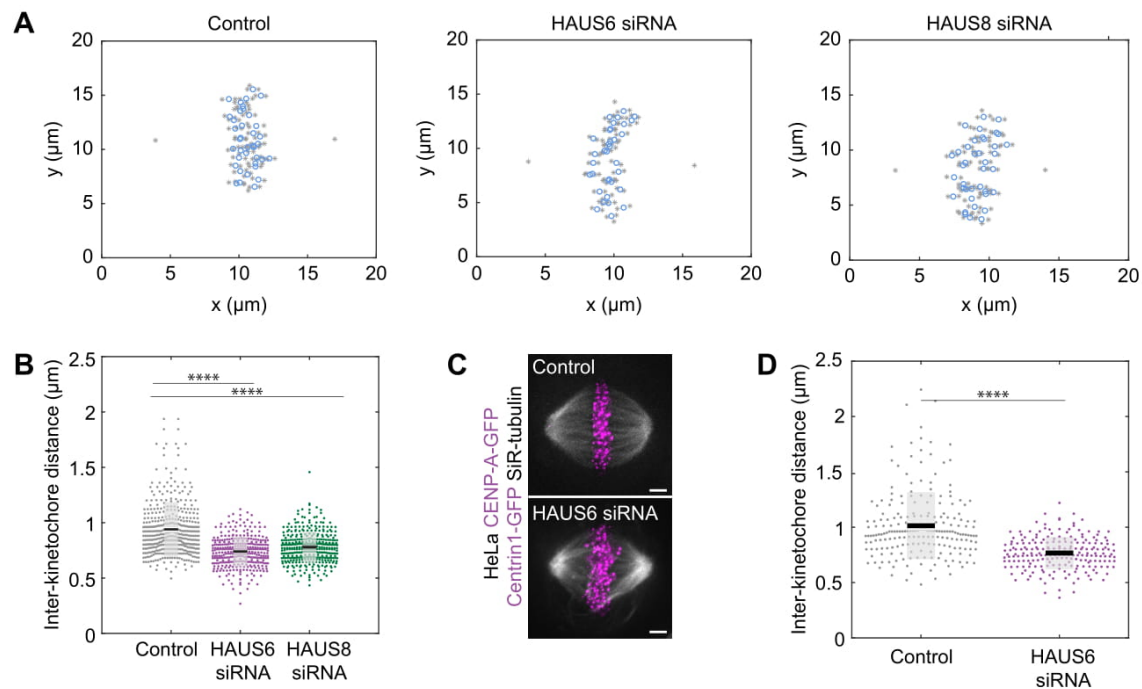
	hTERT-RPE1 cells stably expressing CENP-A-GFP and centrin1-GFP			HeLa cells stably expressing PRC1-GFP		
	Control	HAUS6 siRNA	HAUS8 siRNA	Control	HAUS6 siRNA	HAUS8 siRNA
Spindle length ( $\mu$ m)	13.5 $\pm$ 0.3	11.8 $\pm$ 0.3	11.7 $\pm$ 0.2	11.3 $\pm$ 0.2	13.5 $\pm$ 0.3	11.9 $\pm$ 0.2
Spindle width ( $\mu$ m)	9.5 $\pm$ 0.1	13.0 $\pm$ 0.3	11.8 $\pm$ 0.3	8.4 $\pm$ 0.1	10.2 $\pm$ 0.3	10.0 $\pm$ 0.3
Metaphase plate diameter ( $\mu$ m)	9.5 $\pm$ 0.1	9.4 $\pm$ 0.1	9.3 $\pm$ 0.2	13.6 $\pm$ 0.2	13.3 $\pm$ 0.3	13.1 $\pm$ 0.2

## Supplementary Figures

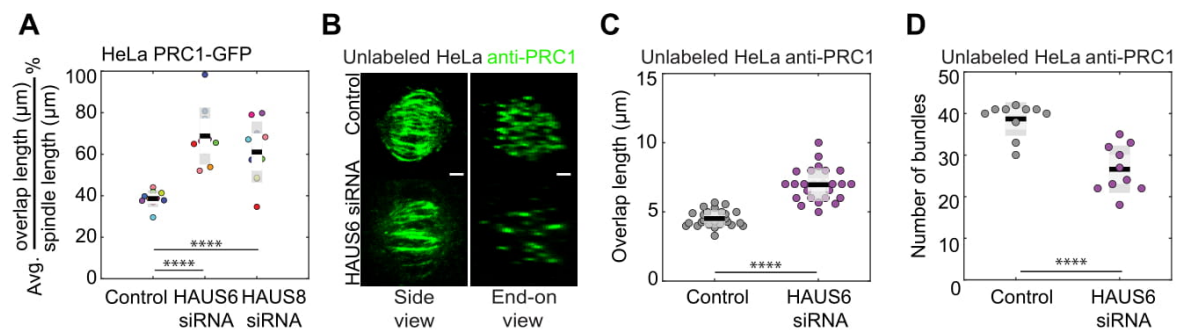


**Supplementary Figure 1 (S1).** (A) Fixed control and HAUS6 siRNA-treated HeLa cells stably expressing PRC1-GFP (green) and immunostained for HAUS6 (magenta). Images are sum intensity projections of five central z-planes. (B) Univariate scatter plot of HAUS6 intensity in control cells (gray) and cells depleted of HAUS6 (magenta). (C) Univariate scatter plot of the tubulin intensities of bridging and k-fibers in control (gray) RPE1 cells stably

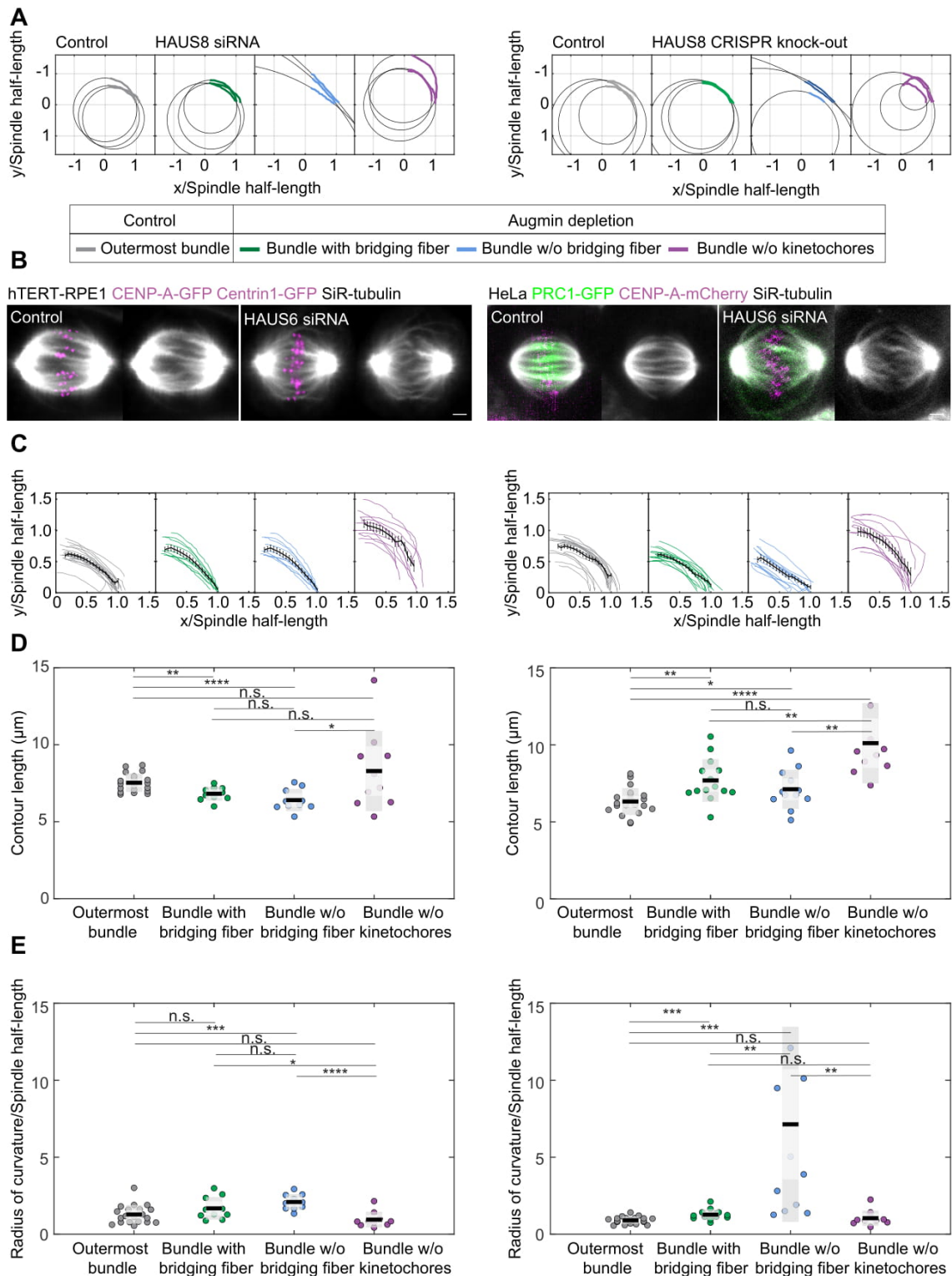
expressing CENP-A-GFP and centrin1-GFP and stained with SiR-tubulin and upon HAUS6 (magenta) and HAUS8 (green) depletion. Schematic representation of the method for measuring the tubulin intensity of a bridging fiber and corresponding k-fibers (kinetochores are shown in magenta and tubulin signal in gray). For the analysis, the average of two k-fibers is calculated and the average of background is subtracted from the tubulin intensity values of the bridging and k-fiber. Boxes represent standard deviation (dark gray), 95% confidence interval of the mean (light gray) and mean value (black). (D) Profile intensities of SiR-tubulin (magenta) and GFP-tubulin (cyan) signals in HeLa GFP- $\alpha$ -tubulin (cyan) cells stained with SiR-tubulin (magenta). The values of two intensity profiles are adjusted to observe the level of overlapping between them and the minimum of the SiR-tubulin signal is set as a distance zero. Statistical analysis; t-test (B and C), p-value legend: < 0.0001 (\*\*\*\*), 0.0001 to 0.001 (\*\*\*), 0.001 to 0.01 (\*\*), 0.01 to 0.05 (\*),  $\geq$  0.05 (ns). Scale bars, 2  $\mu$ m.



**Supplementary Figure 2 (S2).** (A) Coordinates of tracked kinetochore pairs (gray) in control (left) and in HAUS6 (middle) and HAUS8 (right) siRNA-treated hTERT-RPE1 cells stably expressing CENP-A-GFP and centrin1-GFP. The sister kinetochore midpoint is shown as a blue circle and single asterisks denote positions of spindle poles and limits of the metaphase plate. (B) Univariate scatter plot of interkinetochore distance in hTERT-RPE1 cells stably expressing CENP-A-GFP and centrin1-GFP. The interkinetochore distance decreased from  $0.99 \pm 0.04 \mu\text{m}$  in control cells to  $0.73 \pm 0.01 \mu\text{m}$  and  $0.78 \pm 0.01 \mu\text{m}$  in HAUS6 and HAUS8 siRNA-treated cells, respectively ( $N > 400$  kinetochore pairs,  $n=10$  cells for each treatment). (C) HeLa cells stably expressing CENP-A-GFP and centrin1-GFP (both in magenta) stained with SiR-tubulin (gray) in control cells (top) and in cells following HAUS6 depletion (bottom). (D) Univariate scatter plot of interkinetochore distance in HeLa cells stably expressing CENP-A-GFP and centrin1-GFP. The interkinetochore distance decreased from  $1.01 \pm 0.02 \mu\text{m}$  in control cells to  $0.77 \pm 0.01 \mu\text{m}$  following HAUS6 siRNA treatment ( $N > 200$  kinetochore pairs,  $n = 5$  cells). Boxes represent standard deviation (dark gray), 95% confidence interval of the mean (light gray) and mean value (black). Statistical analysis (B and D); t-test, p-value legend:  $< 0.0001$  (\*\*\*\*),  $0.0001$  to  $0.001$  (\*\*\*),  $0.001$  to  $0.01$  (\*\*),  $0.01$  to  $0.05$  (\*),  $\geq 0.05$  (ns). Scale bars, 2  $\mu\text{m}$ .



**Supplementary Figure 3 (S3).** (A) Univariate scatter plot of average overlap length compared to spindle length in HeLa cell line stably expressing PRC1-GFP and stained with SiR-DNA. (B) Fixed control and HAUS6 siRNA-treated unlabeled HeLa cells immunostained for PRC1 (green). Images are sum intensity projections of five central z-planes in a side view and sum projection of ten central z-planes in an end-on view. Corresponding overlap lengths (C) and number of bundles (D) shown in an univariate scatter plot. (E) Boxes represent standard deviation (dark gray), 95% confidence interval of the mean (light gray) and mean value (black). Statistical analysis; t-test, p-value legend: < 0.0001 (\*\*\*\*), 0.0001 to 0.001 (\*\*\*), 0.001 to 0.01 (\*\*), 0.01 to 0.05 (\*),  $\geq 0.05$  (ns). Scale bars, 2  $\mu\text{m}$ .



**Supplementary Figure 4 (S4).** (A) Examples of circle-fitting analysis to determine the curvature of bundles in HAUS8 siRNA-treated RPE1 cells stably expressing CENP-A-GFP and Centrin1-GFP (left) and hTERT-RPE1 cells with induced CRISPR/Cas9/HAUS8 knock-out (right). Outermost bundle (gray) in non-induced cells and bundle with the bridging fiber (green), bundle without the bridging fiber (blue) and bundle without kinetochores (magenta)



in induced cells. (B) Left panel - live images (maximum projection of 3 central z-planes) of metaphase spindles in control and HAUS6 siRNA-treated SiR-tubulin (gray) stained RPE1 cells stably expressing CENP-A-GFP and Centrin1-GFP (both in magenta) and right panel – live images (maximum projection of 3 central z-planes) of metaphase spindles in control and HAUS6 siRNA-treated SiR-tubulin (gray) stained HeLa cells stably expressing PRC1-GFP (green) and CENP-A-mCherry (magenta). (C) Bundle contours in cells from (B); black lines show mean  $\pm$  SEM. (D) Univariate scatter plot of contour lengths and (E) radii of curvature. Boxes represent standard deviation (dark gray), 95% confidence interval of the mean (light gray) and mean value (black). (C-E) Left panel shows results for RPE1 cells stably expressing CENP-A-GFP and Centrin1-GFP in control cells and in cells following HAUS6 depletion. Right panel shows results for HeLa cells stably expressing PRC1-GFP and CENP-A-mCherry in control cells and in cells following HAUS6 depletion. Statistical analysis; t-test, p-value legend:  $< 0.0001$  (\*\*\*\*),  $0.0001$  to  $0.001$  (\*\*\*),  $0.001$  to  $0.01$  (\*\*),  $0.01$  to  $0.05$  (\*),  $\geq 0.05$  (ns). Scale bars,  $2\ \mu\text{m}$ .

**Supplementary Video 1.** SiR-tubulin (gray) stained hTERT-RPE1 cells stably expressing CENP-A-GFP and centrin1-GFP (both in magenta) in 11 single Z-planes ( $\Delta z = 0.5\ \mu\text{m}$ ). The video shows control (left), and cells depleted of HAUS6 (middle) and HAUS8 (right). The video corresponds to still images from Fig. 1B. Scale bar,  $2\ \mu\text{m}$ .

**Supplementary Video 2.** Enlarged metaphase midzone of SiR-tubulin (gray) stained hTERT-RPE1 cells stably expressing CENP-A-GFP and centrin1-GFP (both in magenta). Video shows 11 single Z-planes ( $\Delta z = 0.5\ \mu\text{m}$ ) of control (left), HAUS6 (middle) and HAUS8 (right) depleted cells. Scale bar,  $2\ \mu\text{m}$

**Supplementary Video 3.** HeLa cells stably expressing PRC1-GFP (green) and stained with SiR-DNA (magenta) for chromosomes. Video shows the side view (left) of 21 single Z-planes ( $\Delta z = 0.5\ \mu\text{m}$ ) in control (top), HAUS6 (middle) and HAUS8 (bottom) siRNA-treated cells, as well as corresponding end-on views (right). Side view spindles are smoothed with 0.5-pixel-sigma Gaussian blur. Scale bar,  $2\ \mu\text{m}$ .

**Supplementary Video 4.** hTERT-RPE1 cells with induced CRISPR/Cas9/HAUS8 knock-out stained with SiR-tubulin (gray) and Hoechst dye (magenta) for chromosomes. Video shows 9 single Z planes ( $\Delta z = 0.5 \mu\text{m}$ ). Scale bar,  $2 \mu\text{m}$ .

**Supplementary Video 5.** Time lapse video of control (left) and HAUS6-depleted (right) hTERT-RPE1 cells stably expressing PA- $\alpha$ -tubulin and stained with SiR-tubulin (magenta) before and after the photoactivation (white). Time, seconds. Scale bar,  $2 \mu\text{m}$ .

## References

- Brust-Mascher, I., Sommi, P., Cheerambathur, D. K., and Scholey, J. M. (2009). Kinesin-5-dependent poleward flux and spindle length control in *Drosophila* embryo mitosis. *Mol Biol Cell*, 20(6), 1749-1762. doi:10.1091/mbc.E08-10-1033
- Buda, R., Vukusic, K., and Tolic, I. M. (2017). Dissection and characterization of microtubule bundles in the mitotic spindle using femtosecond laser ablation. *Methods Cell Biol*, 139, 81-101. doi:10.1016/bs.mcb.2016.11.007
- David, A. F., Roudot, P., Legant, W. R., Betzig, E., Danuser, G., and Gerlich, D. W. (2019). Augmin accumulation on long-lived microtubules drives amplification and kinetochore-directed growth. *The Journal of Cell Biology*, 218(7), 2150-2168. doi:10.1083/jcb.201805044
- Dudka, D., Noatynska, A., Smith, C. A., Liaudet, N., McAinsh, A. D., and Meraldi, P. (2018). Complete microtubule-kinetochore occupancy favours the segregation of merotelic attachments. *Nature Communications*, 9. doi:10.1038/s41467-018-04427-x
- Elting, M. W., Prakash, M., Udy, D. B., and Dumont, S. (2017). Mapping Load-Bearing in the Mammalian Spindle Reveals Local Kinetochore Fiber Anchorage that Provides Mechanical Isolation and Redundancy. *Current Biology*, 27(14), 2112-2122.e2115. doi:10.1016/j.cub.2017.06.018
- Ganem, N. J., Upton, K., and Compton, D. A. (2005). Efficient mitosis in human cells lacking poleward microtubule flux. *Current Biology*, 15(20), 1827-1832. doi:10.1016/j.cub.2005.08.065
- Goshima, G., Mayer, M., Zhang, N., Stuurman, N., and Vale, R. D. (2008). Augmin: a protein complex required for centrosome-independent microtubule generation within the spindle. *The Journal of Cell Biology*, 181(3), 421-429. doi:10.1083/jcb.200711053
- Goshima, G., Wollman, R., Goodwin, S. S., Zhang, N., Scholey, J. M., Vale, R. D., and Stuurman, N. (2007). Genes required for mitotic spindle assembly in *Drosophila* S2 cells. *Science*, 316(5823), 417-421. doi:10.1126/science.1141314
- Hayward, D., Metz, J., Pellacani, C., and Wakefield, J. G. (2014). Synergy between multiple microtubule-generating pathways confers robustness to centrosome-driven mitotic spindle formation. *Developmental cell*, 28(1), 81-93. doi:10.1016/j.devcel.2013.12.001
- Jagrić, M., Risteski, P., Jelena, M., Milas, A., and Tolić, I. M. (2020). Optogenetic control of PRC1 reveals that bridging fibers promote chromosome alignment by overlap length-dependent forces. *bioRxiv*.
- Kajtez, J., Solomatina, A., Novak, M., Polak, B., Vukušić, K., Rüdiger, J., Cojoc, G., Milas, A., Šumanovac Šestak, I., Risteski, P., Tavano, F., Klemm, A. H., Roscioli, E., Welburn, J., Cimini, D., Glunčić, M., Pavin, N., and Tolić, I. M. (2016). Overlap microtubules link sister k-fibres and balance the forces on bi-oriented kinetochores. *Nature Communications*, 7(1), 10298. doi:10.1038/ncomms10298
- Kamasaki, T., O'Toole, E., Kita, S., Osumi, M., Usukura, J., McIntosh, J. R., and Goshima, G. (2013). Augmin-dependent microtubule nucleation at microtubule walls in the spindle. *The Journal of Cell Biology*, 202(1), 25-33. doi:10.1083/jcb.201304031
- Kirschner, M. and Mitchison, T. J. (1986). Beyond self-assembly: from microtubules to morphogenesis. *Cell*, 45(3), 329-342. doi:10.1016/0092-8674(86)90318-1
- Lampson, M. A., and Grishchuk, E. L. (2017). Mechanisms to Avoid and Correct Erroneous Kinetochore-Microtubule Attachments. *Biology-Basel*, 6(1). doi:10.3390/biology6010001
- Lawo, S., Bashkurov, M., Mullin, M., Ferreria, M. G., Kittler, R., Habermann, B., Tagliaferro, A., Poser, I., Hutchins, J. R., Hegemann, B., Pinchev, D., Buchholz, F., Peters, J. M., Hyman, A. A., Gingras, A. C., and Pelletier, L. (2009). HAUS, the 8-subunit human Augmin complex, regulates centrosome and spindle integrity. *Curr Biol*, 19(10), 816-826. doi:10.1016/j.cub.2009.04.033
- Li, J., Dallmayer, M., Kirchner, T., Musa, J., and Grunewald, T. G. P. (2018). PRC1: Linking Cytokinesis, Chromosomal Instability, and Cancer Evolution. *Trends Cancer*, 4(1), 59-73. doi:10.1016/j.trecan.2017.11.002
- Mastronarde, D. N., McDonald, K. L., Ding, R., and McIntosh, J. R. (1993). Interpolar spindle microtubules in PTK cells. *J Cell Biol*, 123(6), 1475-1489. doi: 10.1083/jcb.123.6.1475
- McDonald, K. L., O'Toole, E. T., Mastronarde, D. N., and McIntosh, J. R. (1992). Kinetochore microtubules in PTK cells. *The Journal of Cell Biology*, 118(2), 369-383. doi:10.1083/jcb.118.2.369
- Mitchison, T. J. (2005). Mechanism and function of poleward flux in *Xenopus* extract meiotic spindles. *Philos Trans R Soc Lond B Biol Sci*, 360(1455), 623-629. doi:10.1098/rstb.2004.1616
- Miyamoto, D. T., Perlman, Z. E., Burbank, K. S., Groen, A. C., and Mitchison, T. J. (2004). The kinesin Eg5 drives poleward microtubule flux in *Xenopus laevis* egg extract spindles. *J Cell Biol*, 167(5), 813-818. doi:10.1083/jcb.200407126

- Mollinari, C., Kleman, J. P., Jiang, W., Schoehn, G., Hunter, T., and Margolis, R. L. (2002). PRC1 is a microtubule binding and bundling protein essential to maintain the mitotic spindle midzone. *J Cell Biol*, 157(7), 1175-1186. doi:10.1083/jcb.200111052
- Musacchio, A., and Salmon, E. D. (2007). The spindle-assembly checkpoint in space and time. *Nature Reviews Molecular Cell Biology*, 8(5), 379-393. doi:10.1038/nrm2163
- Nicklas, R. B., Ward, S. C., and Gorbsky, G. J. (1995). Kinetochore Chemistry Is Sensitive to Tension and May Link Mitotic Forces to a Cell-Cycle Checkpoint. *Journal of Cell Biology*, 130(4), 929-939. doi:10.1083/jcb.130.4.929
- Novak, M., Polak, B., Simunić, J., Boban, Z., Kuzmić, B., Thomae, A. W., Tolić, I. M., and Pavin, N. (2018). The mitotic spindle is chiral due to torques within microtubule bundles. *Nature Communications*, 9(1), 3571. doi:10.1038/s41467-018-06005-7
- O'Toole, E., Morpew, M., and McIntosh, J. R. (2020). Electron tomography reveals aspects of spindle structure important for mechanical stability at metaphase. *Mol Biol Cell*, 31(3), 184-195. doi:10.1091/mbc.E19-07-0405
- Pavin, N., and Tolić, I. M. (2016). Self-Organization and Forces in the Mitotic Spindle. *Annual Review of Biophysics*, 45(1), 279-298. doi:10.1146/annurev-biophys-062215-010934
- Petry, S., Groen, A. C., Ishihara, K., Mitchison, T. J., and Vale, R. D. (2013). Branching microtubule nucleation in *Xenopus* egg extracts mediated by augmin and TPX2. *Cell*, 152(4), 768-777. doi:10.1016/j.cell.2012.12.044
- Petry, S., Pugieux, C., Nedelec, F. J., and Vale, R. D. (2011). Augmin promotes meiotic spindle formation and bipolarity in *Xenopus* egg extracts. *Proceedings of the National Academy of Sciences of the United States of America*, 108(35), 14473-14478. doi:10.1073/pnas.1110412108
- Polak, B., Risteski, P., Lesjak, S., and Tolić, I. M. (2017). PRC-1 labeled microtubule bundles and kinetochore pairs show one-to-one association in metaphase. *EMBO Reports*, 18(2), 217-230. doi:10.15252/embr.201642650
- Prosser, S. L., and Pelletier, L. (2017). Mitotic spindle assembly in animal cells: a fine balancing act. *Nature Reviews Molecular Cell Biology*, 18(3), 187-201. doi:10.1038/nrm.2016.162
- Simunić, J., and Tolić, I. M. (2016). Mitotic Spindle Assembly: Building the Bridge between Sister K-Fibers. *Trends in Biochemical Sciences*, 41(10), 824-833. doi:10.1016/j.tibs.2016.07.004
- Song, J.-G., King, M. R., Zhang, R., Kadzik, R. S., Thawani, A., and Petry, S. (2018). Mechanism of how augmin directly targets the  $\gamma$ -tubulin ring complex to microtubules. *Journal of Cell Biology*, 217(7), 2417-2428. doi:10.1083/jcb.201711090
- Steblyanko, Y., Rajendraprasad, G., Osswald, M., Eibes, S., Geley, S., Pereira, A. J., Maiato, H., and Barisic, M. (2020). Microtubule poleward flux in human cells is driven by the coordinated action of four kinesins. *bioRxiv*.
- Suresh, P., Long, A. F., and Dumont, S. (2020). Microneedle manipulation of the mammalian spindle reveals specialized, short-lived reinforcement near chromosomes. *eLife*, 9. doi:10.7554/eLife.53807
- Taylor, S. S., Ha, E., and McKeon, F. (1998). The human homologue of Bub3 is required for kinetochore localization of Bub1 and a Mad3/Bub1-related protein kinase. *Journal of Cell Biology*, 142(1), 1-11. doi:10.1083/jcb.142.1.1
- Tolic, I. M. (2018). Mitotic spindle: kinetochore fibers hold on tight to interpolar bundles. *Eur Biophys J*, 47(3), 191-203. doi:10.1007/s00249-017-1244-4
- Tolic, I. M., and Pavin, N. (2016). Bridging the gap between sister kinetochores. *Cell Cycle*, 15(9), 1169-1170. doi:10.1080/15384101.2016.1157976
- Uehara, R., and Goshima, G. (2010). Functional central spindle assembly requires de novo microtubule generation in the interchromosomal region during anaphase. *J Cell Biol*, 191(2), 259-267. doi:10.1083/jcb.201004150
- Uehara, R., Kamasaki, T., Hiruma, S., Poser, I., Yoda, K., Yajima, J., Gerlich, D. W., and Goshima, G. (2016). Augmin shapes the anaphase spindle for efficient cytokinetic furrow ingression and abscission. *Mol Biol Cell*, 27(5), 812-827. doi:10.1091/mbc.E15-02-0101
- Uehara, R., Nozawa, R., Tomioka, A., Petry, S., Vale, R. D., Obuse, C., and Goshima, G. (2009). The augmin complex plays a critical role in spindle microtubule generation for mitotic progression and cytokinesis in human cells. *Proceedings of the National Academy of Sciences*, 106(17), 6998-7003. doi:10.1073/pnas.0901587106
- Verma, V., and Maresca, T. J. (2019). Direct observation of branching MT nucleation in living animal cells. *The Journal of Cell Biology*, 218(9), 2829-2840. doi:10.1083/jcb.201904114

- Vukušić, K., Buđa, R., Bosilj, A., Milas, A., Pavin, N., and Tolić, I. M. (2017). Microtubule Sliding within the Bridging Fiber Pushes Kinetochore Fibers Apart to Segregate Chromosomes. *Developmental Cell*, 43(1), 11-23.e16. doi:10.1016/j.devcel.2017.09.010
- Waters, J. C., Skibbens, R. V., and Salmon, E. D. (1996). Oscillating mitotic newt lung cell kinetochores are, on average, under tension and rarely push. *Journal of Cell Science*, 109, 2823-2831.
- Wu, G., Lin, Y., Wei, R., Chen, Y., Shan, Z., and Lee, W. (2008). Hice1, a novel microtubule-associated protein required for maintenance of spindle integrity and chromosomal stability in human cells. *Molecular and Cellular Biology*, 28(11), 3652-3662. doi:10.1128/MCB.01923-07
- Zhu, H., Copping, J. A., Jang, C.-Y., Yates, J. R., and Fang, G. (2008). FAM29A promotes microtubule amplification via recruitment of the NEDD1-gamma-tubulin complex to the mitotic spindle. *The Journal of Cell Biology*, 183(5), 835-848. doi:10.1083/jcb.200807046